

# The AMIGO1 adhesion protein activates Kv2.1 voltage sensors

Condensed Title: AMIGO1 activates Kv2.1 voltage sensors

R.J. Sepela<sup>1</sup>, R.G. Stewart<sup>1</sup>, L.A. Valencia<sup>3</sup>, P. Thapa<sup>1</sup>, Z. Wang<sup>3</sup>, B.E. Cohen<sup>3,4</sup>, J.T. Sack<sup>1,2\*</sup>

## 1 Abstract

2 Kv2 voltage-gated potassium channels are modulated by AMIGO neuronal adhesion  
3 proteins. Here, we identify steps in the conductance activation pathway of Kv2.1 channels that  
4 are modulated by AMIGO1 using voltage clamp recordings and spectroscopy of heterologously  
5 expressed Kv2.1 and AMIGO1 in mammalian cell lines. AMIGO1 speeds early voltage sensor  
6 movements and shifts the gating charge–voltage relationship to more negative voltages. The  
7 gating charge–voltage relationship indicates that AMIGO1 exerts a larger energetic effect on  
8 voltage sensor movement than apparent from the midpoint of the conductance–voltage  
9 relationship. When voltage sensors are detained at rest by voltage sensor toxins, AMIGO1 has a  
10 greater impact on the conductance–voltage relationship. Fluorescence measurements from  
11 voltage sensor toxins bound to Kv2.1 indicate that with AMIGO1, the voltage sensors enter their  
12 earliest resting conformation, yet this conformation is less stable upon voltage stimulation. We  
13 conclude that AMIGO1 modulates the Kv2.1 conductance activation pathway by destabilizing  
14 the earliest resting state of the voltage sensors.

## 15 Statement of Significance

16 Kv2 potassium channels activate a potassium conductance that shapes neuronal action  
17 potentials. The AMIGO family of adhesion proteins modulate activation of Kv2 conductances,  
18 yet, which activation steps are modified is unknown. This study finds that AMIGO1 destabilizes  
19 the earliest resting conformation of the Kv2.1 voltage sensors to promote activation of channel  
20 conductance.

## 21 Introduction

22 Voltage-gated potassium (Kv) channels of the Kv2 family open following membrane  
23 depolarization and are critical regulators of neuronal electrical excitability. Mammals have two  
24 Kv2 pore-forming  $\alpha$  subunits, Kv2.1 and Kv2.2, which function as homo- or heterotetramers (1).  
25 The molecular architecture of Kv2 channels is similar to Kv1 channels for which atomic  
26 resolution structures have been solved (2). Each  $\alpha$  subunit monomer has six transmembrane  
27 helical segments, S1-S6. S1-S4 comprise a voltage sensor domain (VSD) while S5 and S6  
28 together form one quarter of the central pore domain. In response to sufficiently positive  
29 intracellular voltages, gating charges within the VSD translate from an intracellular resting  
30 position to a more extracellular activated conformation. This gating charge movement powers  
31 the conformational changes of voltage sensor activation, which are coupled to subsequent pore  
32 opening and  $K^+$  conduction (3). Kv channels progress through a landscape of conformations  
33 leading to opening, all of which define a pathway for the activation of the  $K^+$  conductance. The  
34 activation pathway of Kv2 channels is distinct from Kv1 channels, as Kv2.1 channels have a  
35 pore opening step which is slower and more weakly voltage-dependent than the VSD movement  
36 of Kv1 channels (3–5). The unique kinetics and voltage dependence of Kv2 currents are critical  
37 to neuronal activity, as they regulate action potential duration and can either support or limit  
38 repetitive firing (6–10).

39 Kv2 channels are abundant in most mammalian central neurons (11). Genetic deletion of  
40 Kv2.1 leads to seizure susceptibility and behavioral hyperexcitability in mice (12), and human  
41 Kv2.1 mutations result in developmental epileptic encephalopathy (13–15), underscoring the  
42 importance of these channels to brain function. Homeostatic Kv2.1 regulation maintains  
43 neuronal excitability (16). Kv2.1 regulation by ischemia (17, 18), glutamate (19),

44 phosphorylation (20) and SUMOylation (21) and AMIGO auxiliary subunits (22, 23) all shift the  
45 midpoint of the conductance–voltage relation ( $G$ – $V$ ). However, it is not known which steps in the  
46 conductance activation pathway are modulated by any of these forms of regulation.

47 To identify steps in the Kv2.1 conduction activation pathway that are susceptible to  
48 modulation, we studied the impact of an AMIGO auxiliary subunit. The AMIGO (AMphoterin–  
49 Induced Gene and Open reading frame) family of proteins contains three paralogs in mammals:  
50 AMIGO1, AMIGO2, and AMIGO3. AMIGO proteins are single-pass transmembrane proteins  
51 with an extracellular immunoglobulin domain and several leucine-rich repeats (24). AMIGO1  
52 has been proposed to play a role in schizophrenia biology (25). In vertebrate brain neurons,  
53 AMIGO1 is important for cell adhesion (24), neuronal tract development (26), and circuit  
54 formation (25–27). AMIGO1 colocalizes with Kv2 in neurons throughout the brains of multiple  
55 mammalian species (22, 28). Coimmunoprecipitation of AMIGO1 and Kv2.1 (22, 23, 26) and  
56 co-diffusion through cell membranes (22) indicate a robust interaction, consistent with an  
57 AMIGO1–Kv2.1 complex being sufficiently stable for intensive biophysical studies. All three  
58 AMIGO proteins activate the conductance of both Kv2 channel subtypes, shifting the  
59 conductance–voltage relation by -5 to -15 mV (22, 23). While these shifts may seem small in  
60 excitable cells that can have voltage swings of more than 100 mV, human mutations that shift the  
61 conductance–voltage relation of ion channel gating by similar magnitudes are correlated with  
62 physiological consequences (13, 29–31). However, it is difficult to determine whether the  
63 physiological consequences of mutations are caused by the gating shifts themselves.

64 Here we investigate which steps in the Kv2.1 conductance activation pathway are  
65 modulated by AMIGO1. In other voltage-gated ion channels, the  $G$ – $V$  relation can be shifted to  
66 more negative voltages by modulating pore opening (32–34), voltage sensor movement (35, 36),  
67 or voltage sensor-pore coupling (37–39). Single-pass transmembrane auxiliary subunits modulate  
68 other voltage-gated ion channel  $\alpha$  subunits by a variety of mechanisms (32, 38, 40, 41).  
69 However, AMIGO1 only shares a limited degree of homology with other single-pass  
70 transmembrane auxiliary subunits (42), and divergent structural interactions have been observed  
71 among single-pass transmembrane auxiliary subunits (43, 44). As there is no consensus binding  
72 pose or mechanism of interaction for auxiliary subunits, it is difficult to predict on which step in  
73 the conductance activation pathway AMIGO1 acts. A recent study proposed that AMIGO  
74 proteins shift Kv2.1 conductance by increasing voltage sensor-pore coupling and that AMIGO-  
75 conferred changes to Kv2 voltage-sensing machinery are unlikely (23). Here we ask whether  
76 AMIGO1 alters conformational changes associated with pore opening or with voltage sensor  
77 movement using a combination of electrophysiological and imaging approaches. We find that  
78 AMIGO1 modulates voltage sensor movements which occur before pore opening. We find  
79 AMIGO1 to have a greater impact on early voltage sensor movements than the conductance–  
80 voltage relation. We conclude that AMIGO1 destabilizes the earliest resting conformation in the  
81 pathway of channel activation.

## 82 Methods

### 83 GxTX peptides

84 A conjugate of a cysteine-modified guangxitoxin-1E and the maleimide of fluorophore Alexa594 (GxTX  
85 Ser13Cys(Alexa594)) was used to selectively modulate Kv2.1 channel gating and to fluorescently identify surface-  
86 expressing Kv2.1 channels (45). Conjugates of propargylglycine (Pra)-modified GxTX and the fluorophore JP-N<sub>3</sub>  
87 (GxTX Ser13Pra(JP) and GxTX Lys27Pra(JP)) were used to monitor the chemical environment surrounding GxTX  
88 when localized to the channel (46). All modified GxTX-mutants were synthesized by solid phase peptide synthesis  
89 as described (46–48). Stock solutions were stored at -80 °C and thawed on ice on the day of experiment.  
90

### 91 Cell culture and transfection

92 The HEK293 cell line subclone TS201A was a gift from Vladimir Yarov-Yarovoy and was maintained in  
93 DMEM (Gibco Cat# 11995-065) with 10% Fetal Bovine Serum (HyClone, SH30071.03HI, LotAXM55317) and 1%  
94 penicillin/streptomycin (Gibco, 15-140-122) in a humidified incubator at 37°C under 5% CO<sub>2</sub>. Chinese Hamster  
95 Ovary (CHO) cell lines were a Tetracycline-Regulated Expression (T-REx) variant (Invitrogen, Cat# R71807), and  
96 cultured as described previously (47). The Kv2.1-CHO cell subclone (49) was stably transfected with pCDNA4/TO  
97 encoding the rat Kv2.1 (rKv2.1) channel. Cell lines were negative for mycoplasma by biochemical test (Lonza,  
98 LT07). 1 µg/ml minocycline (Enzo Life Sciences), prepared in 70% ethanol, was added to Kv2.1-CHO cells to  
99 induce rKv2.1 channel expression for 1.5 hours to minimize series resistance-induced voltage errors in K<sup>+</sup> current  
100 recordings or for 48 hours to produce sufficient Kv2.1 density necessary for recording gating currents. 5 minutes  
101 prior to transfection, cells were plated at 40% confluency in unsupplemented culture media free of antibiotics,  
102 selection agents, and serum and allowed to settle at room temperature. For imaging studies (except concentration-  
103 response), cells were plated in 35 mm No. 1.5 glass-bottom dishes (MatTek, P35G-1.5-20-C). For concentration-  
104 response time-lapse imaging, cells were plated onto 22 x 22 mm No. 1.5H cover glass (Deckglaser). For  
105 electrophysiological studies, cells were plated in 35 mm tissue culture treated polystyrene dishes (Fisher Scientific,  
106 12-556-000). Transfections were achieved with Lipofectamine 2000 (Life Technologies, 11668-027). Each  
107 transfection included 220 µL Opti-MEM (Life Technologies, 31985062), 1.1 µL Lipofectamine, and the following  
108 amount of plasmid DNA. HEK293 cell experiments: 0.1 µg of mKv2.1 DNA and either 0.1 µg of pEGFP,  
109 mAMIGO1-pIRES2-GFP DNA, or hSCN1β-pIRES2-GFP. The pIRES2-GFP vector has an encoded internal  
110 ribosome entry site which promotes continuous translation of two genes from a singular mRNA (50) so that GFP  
111 fluorescence indicates the presence of AMIGO1 or SCN1β mRNA. Kv2.1-CHO cell experiments: 1 µg of either  
112 mAMIGO1-pEYFP-N1, pEGFP, rAMIGO2-pEYFP-N1, or rAMIGO3-pEYFP-N1. CHO cell experiments: 1 µg  
113 of both pCAG-ChroME-mRuby2-ST and mAMIGO1-pEYFP-N1. Cells were incubated in the transfection cocktail  
114 and 2 mL of unsupplemented media for 6-8 hours before being returned to regular growth media, and used for  
115 experiments 40-48 hours after transfection. pEGFP, mAMIGO1-pEYFP-N1, and pCAG-ChroME-mRuby2-ST (51)  
116 plasmids were gifts from James Trimmer. mAMIGO1-pEYFP-N1 uses a VPRARDPPVAT linker to tag the  
117 internal C-terminus of wild-type mouse AMIGO1 (NM\_001004293.2 or NM\_146137.3) with eYFP. pCAG-  
118 ChroME-mRuby2-ST encodes an mRuby2-tagged channelrhodopsin with a Kv2.1 PRC trafficking sequence (51,  
119 52). mKv2.1 (NM\_008420) was purchased from OriGene (MG210968). hSCN1β-pIRES2-GFP was a gift from  
120 Vladimir Yarov-Yarovoy. mAMIGO1 was subcloned into pIRES2-GFP between NheI and BamHI restriction sites.  
121 rAMIGO2-pEYFP-N1 and rAMIGO3-pEYFP-N1 were generated by subcloning rat AMIGO2 (NM\_182816.2) or  
122 rat AMIGO3 (NM\_178144.1) in place of mAMIGO1 in the mAMIGO1-pEYFP-N1 vector.  
123

### 124 Whole-cell K<sup>+</sup> ionic currents

125 Voltage clamp was achieved with an Axopatch 200B patch clamp amplifier (Axon Instruments) run by  
126 Patchmaster (HEKA). Solutions: HEK293 internal (in mM) 160 KCl, 5 EGTA, 10 HEPES, 1 CaCl<sub>2</sub>, 2 MgCl<sub>2</sub>, and  
127 10 glucose, adjusted to pH 7.3 with KOH, 345 mOsm. HEK293 external (in mM) 5 KCl, 160 NaCl, 10 HEPES, 2  
128 CaCl<sub>2</sub>, 2 MgCl<sub>2</sub>, 10 glucose, pH 7.3 with NaOH, 345 mOsm, 5 µM tetrodotoxin added to recording solution: LJP 3.9  
129 mV, E<sub>K</sub>: -89.0 mV with HEK293 internal. Kv2.1-CHO internal (in mM) 70 KCl, 5 EGTA, 50 HEPES, 50 KF, and  
130 35 KOH, adjusted to pH 7.4 with KOH, 310 mOsm. Kv2.1-CHO external (in mM) 3.5 KCl, 155 NaCl, 10  
131 HEPES, 1.5 CaCl<sub>2</sub>, 1 MgCl<sub>2</sub>, adjusted to pH 7.4 with NaOH, 315 mOsm: LJP 8.5 mV, E<sub>K</sub>: -97.4 mV with Kv2.1-  
132 CHO cell internal. High Mg<sup>2+</sup> Kv2.1-CHO external (in mM) 3.5 KCl, 6.5 NaCl, 10 HEPES, 1.5 CaCl<sub>2</sub>, 100 MgCl<sub>2</sub>,  
133 adjusted to pH 7.4 with NaOH, 289 mOsm: LJP 13.1 mV, E<sub>K</sub>: -97.4 mV with Kv2.1-CHO internal. Osmolality  
134 measured with a vapor pressure osmometer (Wescor, 5520), 5% difference between batches were tolerated. Liquid  
135 junction potential (LJP) values were tabulated using Patcher's Power Tools version 2.15 (Max-Planck), and

136 corrected *post hoc*, during analysis. Voltage protocols list command voltages, prior to LJP correction. Kv2.1–CHO  
 137 cells were harvested by scraping in Versene (Gibco, 15040066) or TrypLE (Gibco, 12563011). HEK293 cells were  
 138 dislodged by scraping. Cells were washed three times in a polypropylene tube in the external solution used in the  
 139 recording chamber bath by pelleting at 1,000 x *g* for 2 min, and rotated at room temperature (22–24 °C) until  
 140 use. Cells were then pipetted into a 50  $\mu$ L recording chamber (Warner Instruments, RC-24N) and allowed to settle  
 141 for 5 or more minutes. After adhering to the bottom of the glass recording chamber, cells were rinsed with external  
 142 solution using a gravity–driven perfusion system. Cells showing plasma membrane-associated YFP, or intracellular  
 143 GFP of intermediate intensity, were selected for patching. Thin-wall borosilicate glass recording pipettes (BF150-  
 144 110-7.5HP, Sutter) were pulled with blunt tips, coated with silicone elastomer (Sylgard 184, Dow Corning), heat  
 145 cured, and tip fire-polished to resistances less than 4 M $\Omega$ . Series resistance of 3–9 M $\Omega$  was estimated from the  
 146 whole-cell parameters circuit. Series resistance compensation (of < 90%) was used as needed to constrain voltage  
 147 error to less than 10 mV, lag was 10  $\mu$ s. Cell capacitances were 4–15 pF. Capacitance and Ohmic leak were  
 148 subtracted using a P/5 protocol. Output was low-pass filtered at 10 kHz using the amplifier’s built-in Bessel and  
 149 digitized at 100 kHz. Traces were filtered at 2 kHz for presentation. Intersweep interval was 2 s. HEK293 cells with  
 150 less than 65 pA/pF current at +85 mV were excluded to minimize impact of endogenous K<sup>+</sup> currents (53). The  
 151 average current in the final 100 ms at holding potential prior to the voltage step was used to zero-subtract each  
 152 recording. Mean outward current ( $I_{avg,step}$ ) was amplitude between 90–100 ms post depolarization. Mean tail current  
 153 was the current amplitude between 0.2–1.2 ms into the 0 mV step. 100  $\mu$ L of 100 nM GxTX-594 was flowed over  
 154 cells with membrane resistance greater than 1 G $\Omega$ , pulses to 0 mV gauged the time course of binding, and the *G–V*  
 155 protocol was run. Data with predicted voltage error,  $V_{error} \geq 10$  mV was excluded from analysis.  $V_{error}$  was tabulated  
 156 using estimated series resistance post compensation ( $R_{s,post}$ )

$$V_{error} = I_{avg,step} * R_{s,post} \quad (\text{Eqn. A})$$

157 For *G–V* profiles cell membrane voltage ( $V_{membrane}$ ) was adjusted by  $V_{error}$  and *LJP*.

$$V_{membrane} = V_{command} - V_{error} - LJP \quad (\text{Eqn. B})$$

158 Tail currents were normalized by the mean current from 50 to 80 mV. Fitting was carried out using Igor Pro  
 159 software, version 7 or 8 (Wavemetrics, Lake Oswego, OR) that employs nonlinear least squares curve fitting via the  
 160 Levenberg-Marquardt algorithm. To represent the four independent and identical voltage sensors that must all  
 161 activate for channels to open, *G–V* relations were individually fit with a 4<sup>th</sup> power Boltzmann

$$f(V) = A \left( 1 + e^{\frac{-(V-V_{1/2})zF}{RT}} \right)^{-x} \quad (\text{Eqn. C})$$

162 where  $f(V)$  is normalized conductance (*G*), *A* is maximum amplitude, *x* is the number of independent identical  
 163 transitions required to reach full conductance (for a 4<sup>th</sup> power function, *x*=4),  $V_{1/2}$  is activation midpoint, *z* is the  
 164 valence in units of elementary charge ( $e_0$ ), *F* is the Faraday constant, *R* is the ideal gas constant, and *T* is absolute  
 165 temperature. The half-maximal voltage ( $V_{Mid}$ ) for 4<sup>th</sup> power functions is

$$V_{Mid} = V_{i,1/2} + \frac{42.38}{z_i} \quad (\text{Eqn. D})$$

166 Reconstructed Boltzmann curves use average  $z_i$  and  $V_{1/2} \pm$  SD. The minimum Gibbs free energy ( $\Delta G_{AMIGO1}$ ) that  
 167 AMIGO1 imparts to conductance, was tabulated as

$$\Delta G = -R \times T \times \ln(K_{eq}) \quad (\text{Eqn. E})$$

168 Here  $R = 0.00199$  kcal/(K•mol) and  $T = 298$ K.  $K_{eq}$ , or the equilibrium constant of channel opening, was

169 approximated by  $\frac{f_{Kv2.1+AMIGO1}(V_{i,Mid,Kv2.1})}{1-f_{Kv2.1+AMIGO1}(V_{i,Mid,Kv2.1})}$  where  $f_{Kv2.1+AMIGO1}(V_{i,Mid,Kv2.1})$  is the reconstructed relative conductance  
 170 of Kv2.1 + AMIGO1 at  $V_{i,Mid}$  of Kv2.1–control cells (Table 1).

171 Activation time constants ( $\tau_{act}$ ) and sigmoidicity values ( $\sigma$ ) (54) were derived by fitting 10–90% current rise  
 172 with

$$I_K = A \left( 1 - e^{-\frac{t}{\tau_{act}}} \right)^\sigma \quad (\text{Eqn. F})$$

173 Where current at end of step,  $I_{avg,step}$ , was set to 100%.  $t = 0$  was adjusted to 100  $\mu$ s after voltage step start to correct  
 174 for filter delay and cell charging. Deactivation time constants ( $\tau_{deact}$ ) were from fitting 1 to 100 ms of current decay  
 175 during 0 mV tail step with an exponential function

$$I_K = y_0 + A e^{-\frac{t-t_0}{\tau_{deact}}} \quad (\text{Eqn. G})$$

176 Reported  $\tau_{deact}$  was the average after steps to +10 mV to +120 mV or +50 mV to +120 mV in GxTX–594. Kv2.1  
 177 deactivation kinetics became progressively slower after establishment of whole-cell mode, similar to Shaker

178 deactivation after patch excision (55). Due to the increased variability of deactivation kinetics expected from this  
 179 slowing phenomenon, deactivation kinetics were not analyzed further.

180

181 On-cell single channel K<sup>+</sup> currents

182 Single channel recordings were made from on-cell patches, to avoid Kv2.1 current rundown that occurs  
 183 after patch excision (56). Methods same as whole-cell K<sup>+</sup> ionic currents unless noted. While cells selected for  
 184 recording had AMIGO1–YFP fluorescence apparent at the surface membrane, we cannot be certain each single  
 185 Kv2.1 channel interacted with AMIGO1. Solutions: Kv2.1–CHO single channel internal (in mM) 155 NaCl, 50  
 186 HEPES, 20 KOH, 2 CaCl<sub>2</sub>, 2 MgCl<sub>2</sub>, 0.1 EDTA, adjusted to pH 7.3 with HCl, 347 mOsm. Kv2.1–CHO single  
 187 channel external (in mM) 135 KCl, 50 HEPES, 20 KOH, 20 NaOH, 2 CaCl<sub>2</sub>, 2 MgCl<sub>2</sub>, 0.1 EDTA, adjusted to pH  
 188 7.3 with HCl, 346 mOsm: LJP -3.3 mV with Kv2.1–CHO single channel internal. Thick-wall borosilicate glass  
 189 (BF150-86-7.5HP; Sutter Instruments) was pulled, Sylgard-coated and fire-polished, to resistances >10 MΩ.  
 190 Analysis methods were same as prior (5) unless noted. To subtract capacitive transients, traces without openings  
 191 were averaged and subtracted from each trace with single-channel openings. Peaks in single channel amplitude  
 192 histograms were fit to half maximum with a Gaussian function to define single channel opening level for  
 193 idealization by half-amplitude threshold. Open dwell times were well described by a single exponential component  
 194 which was used to derived  $\tau_{\text{closing}}$ . Average open dwell times were also described as the geometric mean of all open  
 195 dwell times. Closed dwell times appeared to have multiple exponential components and were solely described as the  
 196 geometric mean of all closed dwell times.

197

198 Whole-cell gating current measurements

199 Methods same as whole-cell K<sup>+</sup> ionic currents unless noted. Solutions: gating current internal (in mM) 90  
 200 NMDG, 1 NMDG-Cl, 50 HEPES, 5 EGTA, 50 NMDG-F, 0.01 CsCl, adjusted to pH 7.4 with methanesulfonic acid,  
 201 303 mOsm. Gating current external (in mM) 150 TEA-Cl, 41 HEPES, 1 MgCl<sub>2</sub> · 6 H<sub>2</sub>O, 1.5 CaCl<sub>2</sub>, adjusted to  
 202 pH to 7.3 with NMDG, 311 mOsm: LJP -3.3 mV with gating current internal. To avoid KCl contamination of the  
 203 recording solution from the pH electrode, pH was determined in small aliquots that were discarded. Cells were  
 204 resuspended in Kv2.1–CHO external and washed in the recording chamber with 10 mL gating current  
 205 external. Pipettes has resistances of 6-14 MΩ. Series resistances were 14-30 MΩ and compensated 50%. Cell  
 206 capacitances were 6-10 pF.  $V_{\text{error}}$  was negligible (< 1 mV). P/5.9 leak pulses from -133 mV leak holding potential.  
 207 An early component ON gating charge movement was quantified by integrating ON gating currents in a 3.5 ms  
 208 window ( $Q_{\text{ON,fast}}$ ) following the end of fast capacitive artifacts created from the test voltage step (which usually  
 209 concluded 0.1 ms following the voltage step). The slow tail of the ON charge movement is difficult to accurately  
 210 integrate in these cells, making the cutoff point arbitrary. This 3.5 ms integration window resulted in a more positive  
 211  $Q_{\text{ON,fast}}-V$  midpoint than with a 10 ms window (5), and more positive midpoint than the  $G-V$  relation. Differences in  
 212 gating current solutions compared to prior studies may also contribute to the different midpoints reported (4, 5, 57).  
 213 Currents were baseline-subtracted from 4 to 5 ms into step.  $Q_{\text{OFF}}$  was determined by integration of OFF charge  
 214 movement in a 9.95 ms window after capacitive artifacts (usually 0.1 ms). Currents were baseline-subtracted from  
 215 10 to 20 ms into the step. Gating charge density  $fC/pF$  was normalized by cell capacitance.  $Q-V$  curves normalized  
 216 to average from 100-120 mV.  $Q-V$  relations were individually fit with a 1<sup>st</sup> power Boltzmann (Eqn. C.,  $x=1$ ). Time  
 217 constants ( $\tau_{\text{ON}}$ ) were determined from a double-exponential fit function

$$I_{g,\text{ON}} = A \left( e^{\frac{-t}{\tau_{\text{ON}}}} \right) + B - A_{\text{rise}} \left( e^{\frac{-t}{\tau_{\text{rise}}}} \right) \quad (\text{Eqn. H})$$

218  $\tau_{\text{rise}}$  was not used in analyses.  $I_{g,\text{OFF}}$  was not well fit by Eqn. H and  $\tau_{\text{OFF}}$  was not analyzed. The voltage-dependence of  
 219 the forward voltage sensor activation ( $\alpha$ ) rate was determined by fitting the average  $\tau_{\text{ON}}-V$  weighted by the standard  
 220 error

$$\tau_{\text{ON}} = \frac{1}{\alpha_{0\text{mV}} e^{Vz_{\alpha}F/RT} + \beta_{0\text{mV}} e^{Vz_{\beta}F/RT}} \quad (\text{Eqn. I})$$

221 Reverse rates were not analyzed. Energy of AMIGO1 impact on the activation rate of all 4 voltage sensors  
 222 ( $\Delta G^{\ddagger}_{\text{AMIGO1}}$ ) was

$$\Delta G = -4 \times R \times T \times \ln \left( \frac{k_{\text{Kv2.1} + \text{AMIGO1}}}{k_{\text{Kv2.1}}} \right) \quad (\text{Eqn. J})$$

223 where  $k = \alpha_{0\text{mV}}$ . Estimates of  $\Delta G_{\text{AMIGO1}}$  from  $Q-V$  relations were with Eqn. E or

$$\Delta G = V_{1/2} \times Q \times F \quad (\text{Eqn. K})$$

224 Here  $F = 23.06 \text{ kcal/V} \cdot \text{mol} \cdot e_0$ .  $Q$  was either  $z_g$  from fits or  $12.5 e_0$  as determined from a limiting slope analysis of  
225 the Kv2.1 open probability-voltage relation (3).  $V_{1/2}$  was either  $V_{g, \text{Mid}}$  or a median voltage ( $V_{g, \text{Med}}$ ) as calculated from  
226 integration above and below  $Q_{\text{OFF}}-V$  relations using a trapezoidal rule (58).

227

## 228 Fluorescence imaging

229 Images were obtained with an inverted confocal/airy disk imaging system with a diffraction grating  
230 separating 400-700 nm emission into 9.6 nm bins (Zeiss LSM 880, 410900-247-075) run by ZEN black v2.1. Laser  
231 lines were 3.2 mW 488 nm, 1.2 mW 514 nm, 0.36 mW 543 nm, 0.60 mW 594 nm. Images were acquired with a 1.4  
232 NA 63x (Zeiss 420782-9900-799), 1.3 NA 40x (Zeiss 420462-9900-000), or 1.15 NA 63x objectives (Zeiss 421887-  
233 9970-000). Images were taken in either confocal or airy disk imaging mode. The imaging solution was Kv2.1-CHO  
234 external supplemented with 0.1% bovine serum albumin and 10 mM glucose. Temperature inside the microscope  
235 housing was 24-28 °C. Representative images had brightness and contrast adjusted linearly.

236 *Concentration-effect imaging.* Cells plated on coverslips were washed 3x with imaging solution then  
237 mounted on an imaging chamber (Warner Instruments, RC-24E) with vacuum grease. 100  $\mu\text{L}$  GxTX-594 dilutions  
238 were applied for 10 minutes, then washed-out by flushing 10 mL at a flow rate of  $\sim 1 \text{ mL} / 10 \text{ sec}$ . 15 minutes after  
239 wash-out, the next GxTX-594 concentration was added. Airy disk imaging, 1.4 NA 63x objective (Zeiss 420782-  
240 9900-799), 0.13  $\mu\text{m}$  pixels, 0.85  $\mu\text{s}$  dwell, 5 sec frame rate. YFP excitation 488 nm 2% power, emission 495-550  
241 nm. GxTX-594 excitation 594 nm 2% power, emission 495-620 nm. Intensities extracted using FIJI (59). ROIs  
242 drawn around groups of cells  $\pm$  YFP fluorescence. Dissociation constant ( $K_d$ ) fit with fluorescence intensity at 0 nM  
243 GxTX-594 set to 0 with

$$f(x) = A \frac{1}{(1 + K_d/x)} + B \quad (\text{Eqn. L})$$

244 *Voltage clamp fluorimetry* was conducted as described (45). Briefly, 100  $\mu\text{L}$  100 nM GxTX-594 in  
245 imaging external was applied for 10 minutes then diluted with 1 mL Kv2.1-CHO external for imaging. Airy disk  
246 imaging, 1.15 NA 63x objective (Zeiss 421887-9970-000), 0.11  $\mu\text{m}$  pixels, 0.85  $\mu\text{s}$  dwell, 2x averaging, 1 sec frame  
247 rate. GxTX-594 excitation 594 nm 1% power, emission 605nm long-pass. Cells with obvious GxTX-594 labeling  
248 were whole-cell voltage-clamped. Voltage clamp fluorimetry internal (in mM) 70 mM CsCl, 50 mM CsF, 35mM  
249 NaCl, 1 mM EGTA, 10 mM HEPES, adjusted to pH 7.4 with CsOH, 310 mOsm: LJP -5.3 mV with Kv2.1-CHO  
250 external. Pipettes from thin-wall glass were less than 3.0 M $\Omega$ . Cells were held at -100 mV for 30 images and stepped  
251 to +35 mV until fluorescence change appeared complete. Intensity data was extracted using Zen Blue from ROIs  
252 drawn around apparent surface membrane excluding pipette region. For presentation, fluorescence intensity traces  
253 were normalized from minimum to maximum. Rate of GxTX-594 dissociation ( $k_{AF}$ ) was fit with a monoexponential  
254 function (Eqn. G), and  $K_{eq}$  for resting vs. activated voltage sensors was calculated as described (45).  $\Delta G_{\text{AMIGO1}}$  from  
255 with Eqn. J where  $k = K_{eq}$ .

256 *Environment-sensitive fluorescence imaging* with GxTX Ser13Pra(JP) and GxTX Lys27Pra(JP). Cells were  
257 incubated in 100  $\mu\text{L}$  of GxTX(JP) solution for 5-10 minutes then washed with imaging solution. Spectral confocal  
258 imaging, 1.4 NA 63x objective, 0.24  $\mu\text{m}$  pixels, 8.24  $\mu\text{s}$  dwell, 2x averaging. YFP excitation 514 nm. GxTX  
259 Ser13Pra(JP) excitation 594 nm. GxTX Lys27Pra(JP) excitation 543 nm. Fluorescence counts extracted in Zen  
260 Blue. JP emission spectra were fit with two-component split pseudo-Voigt functions (46) using the curve fitting  
261 software Fityk 1.3.1 (<https://fityk.nieto.pl/>), which employed a Levenberg-Marquardt algorithm. Goodness of fit  
262 was determined by root-mean-squared deviation ( $R^2$ ) values, which are listed in Supplemental Table 2 along with  
263 the parameters of each component function. To avoid YFP overlap, fittings for spectra from cells expressing  
264 AMIGO1-YFP include emission data points from 613-700 nm for GxTX Ser13Pra(JP) and 582-700 nm for GxTX  
265 Lys27Pra(JP). Fittings for JP spectra from cells without AMIGO1-YFP included all data from 550-700 nm.

266

## 267 Experimental Design and Statistical Treatment

268 Independent replicates ( $n$ ) are individual cells pooled over multiple transfections. The  $n$  from each  
269 transfection for each figure are listed in Supplemental Tables 3 and 4. In each figure panel, control and test cells  
270 were plated side by side from the same suspensions, transfected side by side, and the data was acquired from control  
271 and test cells in an interleaved fashion. Identity of transfected constructs was blinded during analysis. ANOVA  
272 analysis of transfection- or acquisition date-dependent variance of Boltzmann fit parameters and PCC/COV did not  
273 reveal a dependence, and all  $n$  values were pooled. Statistical tests were conducted with Prism 9 (GraphPad  
274 Software, San Diego, CA), details in figure legends.

## 275 Results

### 276 AMIGO1 shifts the midpoint for activation of Kv2.1 conductance

277 Voltage-clamp recordings from cotransfected HEK293 cells indicate that mouse  
278 AMIGO1 shifts the  $G-V$  relation of mouse Kv2.1 by  $-5.7 \pm 2.3$  mV (SEM) (Supplemental Fig.  
279 1). This shift was similar to the  $-6.1$  mV  $\pm$  1.6 mV shift reported of rat Kv2.1-GFP by human  
280 AMIGO1-mRuby2 (23), and smaller than the  $-15.3$  mV (no error listed) shift of mouse Kv2.1-  
281 GFP by mouse AMIGO1 (22). This small effect of AMIGO1 was similar to the cell-to-cell  
282 variability in our recordings. We suspected that endogenous voltage-activated conductances of  
283 HEK293 cells (53, 60) and variability inherent to transient co-transfection could increase  
284 variability. To minimize possible sources of cell-to-cell variability, further experiments were  
285 with a Chinese Hamster Ovary K1 cell line with inducible rat Kv2.1 expression (Kv2.1-CHO)  
286 transfected with a YFP-tagged mouse AMIGO1. Inducible Kv2.1 expression permits tighter  
287 control of current density (49) and fluorescence tagging of AMIGO1 permits visualization of  
288 protein expression and localization. Unlike HEK293 cells, CHO cells lack endogenous voltage-  
289 gated  $K^+$  currents (61).

290 As expression systems can influence auxiliary protein interactions with ion channels (62-  
291 66), we assessed Kv2.1-AMIGO1 association in these CHO cells. We evaluated two hallmarks  
292 of Kv2.1 and AMIGO1 association: Kv2.1 reorganization of AMIGO1, and AMIGO1 / Kv2.1  
293 colocalization (22, 23, 28).

294 In HEK293 cells, heterologously expressed AMIGO1 localization is intracellular and  
295 diffuse (23, 28). However, when co-expressed with Kv2.1, AMIGO1 reorganizes into puncta  
296 with Kv2.1, similar to the expression patterns in central neurons (23, 28). To determine whether  
297 Kv2.1 reorganizes AMIGO1 in Kv2.1-CHO cells, the degree of AMIGO1-YFP reorganization  
298 was quantified using the Coefficient of Variation (COV), which captures non-uniformity of YFP  
299 localization (67). COV was quantified following the limited 1.5 h Kv2.1 induction period used in  
300 whole-cell and single channel  $K^+$  current recordings and the prolonged 48 h induction period  
301 used for gating current recordings or imaging studies. COVs were compared against an  
302 uninduced control (0 h induction) and against an engineered protein, ChroME-mRuby2, which  
303 contains the Kv2.1 PRC trafficking sequence, but lacks the Kv2.1 voltage sensing and pore  
304 forming domains (51, 52). COVs were evaluated from the glass-adhered, basal membrane where  
305 evidence of reorganization is most notable (Fig. 1). Both  $COV_{1.5h}$  and  $COV_{48h}$  were greater than  
306 the  $COV_{0h}$  or  $COV_{ChroME-mRuby2}$  control. This result is consistent with Kv2.1 and AMIGO1  
307 association in CHO cells.

308 As an additional measure of whether Kv2.1 reorganizes AMIGO1 in Kv2.1-CHO cells,  
309 we assessed AMIGO1-YFP and Kv2.1 colocalization using the Pearson's correlation coefficient  
310 (PCC) (68). Surface-expressing Kv2.1 on live cells was labeled with GxTX  
311 Ser13Cys(Alexa594), a conjugate of a voltage sensor toxin guangxitoxin-1E derivative with a  
312 fluorophore, abbreviated as GxTX-594 (45). As auxiliary subunits can impede binding of toxins  
313 to voltage-gated ion channels (69), we tested whether AMIGO1 impacted GxTX-594 binding to  
314 Kv2.1. Under conditions where AMIGO1 modulates most, if not all, Kv2.1 voltage sensor  
315 movements (Fig. 6, 7), we found no evidence that AMIGO1 impedes GxTX-594 binding to  
316 Kv2.1 (Supplemental Fig. 5). Colocalization between AMIGO1-YFP and GxTX-594 was  
317 apparent as  $PCC_{48h}$ , measured from the glass-adhered basal membrane, was greater than the  
318 negative control,  $PCC_{ChroME-mRuby2}$  (Fig. 2B). With a limited 1.5 h induction, GxTX-594 was  
319 difficult to detect at the glass-adhered membrane, so we moved the confocal imaging plane  
320 further from the cover glass to image Kv2.1 on apical cell surfaces where GxTX-594 labeling

321 was more apparent. On these apical surfaces,  $PCC_{1.5h}$  and  $PCC_{48h}$  were greater than  $PCC_{0h}$  (Fig.  
322 2A), consistent with some colocalization of AMIGO1–YFP and Kv2.1. The weakly significant  
323 increase of the  $PCC_{1.5h}$  compared to  $PCC_{0h}$  is consistent with some colocalization.  
324 Disproportionate expression can skew PCC values (70), and the limited GxTX–594 signal is  
325 expected to depress the  $PCC_{1.5h}$  value. Similarly, the lower  $PCC_{48h}$  values were associated with  
326 either minimal or exceptionally bright AMIGO1–YFP signal. Overall, we see no sign of Kv2.1  
327 channels lacking colocalized AMIGO1 in cells with high levels of AMIGO1 expression.  
328 Altogether, the reorganization and colocalization indicate that AMIGO1–YFP and Kv2.1 interact  
329 in the CHO cells used for  $K^+$  current recordings and for gating current measurements.

330

### 331 AMIGO1 shifts the midpoint of activation of Kv2.1 conductance in CHO cells

332 To determine whether AMIGO1 affected the macroscopic  $K^+$  conductance in Kv2.1–  
333 CHO cells, we conducted whole-cell voltage clamp recordings. Cells were transfected with GFP  
334 (Kv2.1–control cells) or with AMIGO1–YFP (Kv2.1 + AMIGO1 cells) and identified for whole-  
335 cell voltage clamp based on the presence of cytoplasmic GFP fluorescence or plasma membrane-  
336 associated YFP fluorescence, respectively (Fig. 3A). Macroscopic ionic current recordings were  
337 made in whole-cell voltage-clamp mode and  $K^+$  conductance was measured from tail currents  
338 (Fig. 3B, C). In expectation of small AMIGO1 effects relative to cell-to-cell variation, recordings  
339 from control cells and AMIGO1 cells were interleaved during each day of experiments and cell  
340 identity was blinded during analysis.  $G$ – $V$  relations were fit with a 4<sup>th</sup> power Boltzmann function  
341 (Eqn. C) (Fig. 3D, E, F) and average midpoints of half-maximal conduction ( $V_{i,Mid}$ ) and  
342 steepness equivalents ( $z_i$ ) were determined (Table 1). In Kv2.1–control cells, the average  $V_{i,Mid}$   
343 was -1.8 mV (Fig. 3H), consistent with prior reports of  $V_{i,Mid}$  ranging from -3 mV to +8 mV in  
344 CHO cells (4, 23, 47, 71). Cell-to-cell variation in  $V_{i,Mid}$  remained notable between Kv2.1–CHO  
345 cells, with variation in  $V_{i,Mid}$  on par with other reports (see *Discussion/Limitations*). The range of  
346  $V_{i,Mid}$  values of Kv2.1 + AMIGO1 cells overlapped with Kv2.1–control cells (Fig. 3H), yet the  
347 average  $V_{i,Mid}$  was negatively shifted by  $-5.7 \pm 2.2$  mV (SEM), similar to  $\Delta V_{i,Mid}$  from mouse  
348 Kv2.1 in HEK293 cells (Table 1). No effect on  $z_i$  was observed. We also tested AMIGO2 and  
349 AMIGO3 on Kv2.1, and found they colocalize and induce  $\Delta V_{i,Mid}$  shifts similar to those reported  
350 from HEK293 cells by Maverick and colleagues (23) (Supplemental Fig. 3, 4), indicating that the  
351 small  $G$ – $V$  shifts by the AMIGO proteins are robust across different experimental preparations.

352 To test if AMIGO1 also alters the rate of activation of Kv2.1 conductance, we analyzed  
353 activation kinetics. The 10-90% of the rise of Kv2.1 currents following a voltage step (Fig. 3A,  
354 B) was fit with the power of an exponential function (Eqn. F) for sigmoidicity ( $\sigma$ ) which  
355 quantifies delay before current rise, and activation time constant ( $\tau_{act}$ ).  $\sigma$  was not significantly  
356 altered by AMIGO1 (Fig. 3J, L, N), suggesting that the Kv2.1 activation pathway retains a  
357 similar structure with AMIGO1 (5). At a subset of voltages less than +70 mV, AMIGO1  
358 expression accelerated activation, decreasing  $\tau_{act}$  (Fig. 3I, K, M), consistent with results of  
359 Maverick and colleagues (23). Following the +10 to +120 mV activating steps, time constants of  
360 tail current decay at 0 mV were similar to  $\tau_{act}$  at 0 mV (Fig. 3O, Eqn. G). A prior study found no  
361 impact of AMIGO1 on Kv2.1 deactivation kinetics at -40 mV (23), and deactivation is not  
362 studied further here. A model of Kv2.1 activation kinetics suggests that voltage sensor dynamics  
363 influence  $\tau_{act}$  below  $\sim +70$  mV, and that at more positive voltages a slow pore opening step limits  
364 kinetics (5). This analysis suggests that AMIGO1 accelerates activation kinetics only in the  
365 voltage range which is sensitive to voltage sensor dynamics.

## 366 Effects of AMIGO1 on pore opening conformational changes were not apparent in single 367 channel recordings

368 To more directly assess whether the pore opening step of the Kv2.1 activation pathway is  
369 modulated by AMIGO1, we analyzed pore openings of single Kv2.1 channels during 1 s long  
370 recordings to 0 mV (Fig. 4A, B). At 0 mV we expect >85% of all Kv2.1–control voltage sensors  
371 or >95% of all Kv2.1–AMIGO1 voltage sensors (Fig. 6T) to activate in less than 2 ms (Fig. 6N),  
372 such that the majority of single channel openings represent stochastic fluctuations between a  
373 closed and open conformation of the pore. Neither the single channel current amplitude (Fig. 4C,  
374 D, E) nor the intra-sweep open probability (Fig. 4F) were significantly impacted by AMIGO1.  
375 AMIGO1 did not significantly impact the single channel open or closed dwell times (Fig. 4G-L).  
376 These results constrain any impact of AMIGO1 on Kv2.1 pore opening to be smaller than the  
377 variability in these single channel measurements.

## 379 A voltage sensor toxin enhances modulation of AMIGO1 on the Kv2.1 conductance

380 To test whether AMIGO1 modulation is dependent on voltage sensor dynamics, we  
381 altered voltage sensor movement with a voltage sensor toxin. GxTX binds to the voltage sensing  
382 domain of Kv2.1 (72), such that exit from the earliest resting conformation limits opening to  
383 more positive voltages (5). If AMIGO1 modulates voltage sensors, then GxTX might be  
384 expected to amplify the AMIGO1 effect. Alternately, if AMIGO1 acts directly on pore opening,  
385 the AMIGO1 impact on the pore opening equilibrium should persist, regardless of voltage sensor  
386 modulation. To distinguish between these possibilities, we measured AMIGO1 modulation in the  
387 presence of the imaging probe GxTX–594, which modulates Kv2.1 by the same mechanism as  
388 GxTX (45) and has a similar affinity for the resting conformation of Kv2.1 with or without  
389 AMIGO1 (Supplemental Fig. 5). We applied 100 nM GxTX–594 to cells and activated the  
390 Kv2.1 conductance. We note that the 100-ms activating pulses are much shorter than the >2  
391 second time constants of GxTX–594 dissociation at extreme positive voltages (45) and during  
392 these short activating pulses we saw no evidence of GxTX–594 dissociation. The AMIGO1  
393  $\Delta V_{i, \text{Mid}}$  of  $-22.1 \pm 4.8$  (SEM) with GxTX–594 was distinct from the AMIGO1  $\Delta V_{i, \text{Mid}}$  of  $-5.7 \pm$   
394  $2.2$  mV (SEM) without GxTX–594 ( $p = 0.00018$ , unpaired, two-tailed t-test), indicating that  
395 GxTX–594 amplifies the impact of AMIGO1 on Kv2.1 conductance. We did not observe a  
396 significant effect of AMIGO1 on  $\tau_{\text{act}}$  or  $\sigma$  in GxTX–594 (Fig. 5J-N). We calculated the impact  
397 of AMIGO1 on a pore opening equilibrium constant ( $K_{\text{eq}}$ ) at the midpoint of the Kv2.1  $G$ – $V$   
398 relation and found a 3.7-fold bias towards a conducting conformation in 100 nM GxTX–594  
399 versus a 1.4-fold bias under control conditions ( $\Delta G_{\text{AMIGO1}} = -0.77$  versus  $-0.28$  kcal/mol  
400 respectively, Table 1). This result indicates that the impact AMIGO1 has on the Kv2.1  
401 conductance is dependent on the dynamics of the activation path. Further, this result indicates  
402 that AMIGO1 opposes the action of GxTX–594, which stabilizes the earliest resting  
403 conformations of Kv2.1 voltage sensor. We also note that the more dramatic modulation by  
404 AMIGO1 with GxTX–594 verifies that most Kv2.1 channels are modulated by AMIGO1 in this  
405 cell preparation in which only a small impact on  $V_{i, \text{Mid}}$  was observed without GxTX–594 (Fig. 3).  
406

## 407 AMIGO1 facilitates the activation of Kv2.1 voltage sensors

408 To determine if AMIGO1 affects voltage sensor movement, we measured gating currents  
409 ( $I_g$ ), which correspond to movement of Kv2.1 voltage sensors across the transmembrane electric  
410 field. Kv2.1–CHO cells were patch clamped in whole-cell mode in the absence of  $K^+$  (Fig. 6A)

411 and given voltage steps to elicit gating currents (Fig. 6B, C). The resolvable ON gating currents  
412 ( $I_{g,ON}$ ) represent an early component of gating charge movement, but not all of the total gating  
413 charge; the later charge movements, which include any charge associated with the pore opening,  
414 move too slowly for us to resolve accurately in ON measurements (4, 5). If AMIGO1 acts solely  
415 through the pore we would not expect to detect an impact on early components of ON gating  
416 currents which occur before pore opening.

417 At voltages above 50 mV, the charge density translocated over the first 3.5 ms,  $Q_{ON,fast}$ ,  
418 was not significantly different with AMIGO1 (Fig. 6D, E, F), indicating that AMIGO1 did not  
419 alter the total charge translocated during early conformational transitions. However, between -10  
420 mV and +50 mV, Kv2.1-control cells did not move as much gating charge as Kv2.1 + AMIGO1  
421 cells, indicating a shift in gating current activation (Fig. 6F). The shift in voltage dependence was  
422 quantified by fitting  $Q_{ON,fast}-V$  with a Boltzmann (Fig. 6G, H, I) yielding  $\Delta V_{g,Mid,ON,fast}$  of  $-12.8 \pm$   
423  $3.5$  mV (SEM) (Fig. 6K) and a  $\Delta z_{g,ON,fast}$  of  $0.215 \pm 0.058 e_0$  (SEM) (Fig. 6J) (Table 2). This  
424 result indicates that AMIGO1 modulates the early gating charge movement which occurs before  
425 pore opening.

426 To determine whether AMIGO1 modulates the kinetics of early gating charge movement,  
427 we extracted a time constant ( $\tau_{ON}$ ) from the decay phase of  $I_{g,ON}$  that occurs before 10 ms (Fig.  
428 6B top, C top) (Eqn. H) as in (5). In Kv2.1 + AMIGO1 cells, the  $\tau_{ON}-V$  relation shifts to more  
429 negative voltages compared to control (Fig. 6L, M, N). Above +30 mV, the mean  $\tau_{ON}$  for Kv2.1  
430 + AMIGO1 cells was faster than the mean  $\tau_{ON}$  from Kv2.1-control cells (Fig. 6N). Fitting the  
431  $\tau_{ON}-V$  with rate theory equations indicated AMIGO1 accelerates the forward rate of gating  
432 charge movement by 1.7x at neutral voltage and decreases the voltage dependence of this rate by  
433 13% (Fig. 6N). This result indicates that voltage sensors activate faster in the presence of  
434 AMIGO1, consistent with destabilization of the earliest resting conformation of the voltage  
435 sensors by AMIGO1.

436 To measure if AMIGO1 alters the total gating charge movement, we integrated OFF  
437 gating currents ( $I_{g,OFF}$ ) at -140 mV after 100 ms voltage steps (Fig. 6B bottom, C bottom, O, P,  
438 Q). The density of  $Q_{OFF}$  elicited by voltage steps above -10 mV was not significantly different  
439 between Kv2.1-control and Kv2.1 + AMIGO1 cells (Fig. 6Q), indicating that AMIGO1 did not  
440 alter the density of channels expressed, nor the total gating charge per channel. However,  
441 between -25 mV and -10 mV, Kv2.1-control cells did not move as much gating charge as Kv2.1  
442 + AMIGO1 cells, indicating a shift in voltage dependence (Fig. 6Q). Boltzmann fits (Fig. 6R, S,  
443 T), yielded  $\Delta V_{g,Mid,OFF}$  of  $-10.8 \pm 2.4$  mV (SEM) (Fig. 6V) and a  $\Delta z_{g,OFF}$  of  $0.43 \pm 0.20 e_0$  (SEM)  
444 (Fig. 6U) (Table 2), indicating that AMIGO1 shifts total gating charge movement to more  
445 negative voltages. Overall, we find that AMIGO1 affects every aspect of gating current we have  
446 analyzed to a greater degree than the  $K^+$  conductance. As both  $Q_{ON,fast}-V$  and  $\alpha_{0mV}$  measurements  
447 report the gating charge movements out of the earliest resting conformation, these results  
448 indicate that AMIGO1 destabilizes the earliest resting conformation relative to voltage sensor  
449 conformations later in the conduction activation pathway of Kv2.1.

450

#### 451 [AMIGO1 accelerates voltage-stimulated GxTX-594 dissociation](#)

452 To further test the hypothesis that AMIGO1 specifically destabilizes the earliest resting  
453 conformation of Kv2.1 voltage sensors, we probed the stability of this conformation with GxTX-  
454 594 fluorescence. The earliest resting conformation is stabilized by GxTX (5) and when  
455 occupancy of this conformation is decreased by voltage activation, the rate of GxTX-594  
456 dissociation accelerates (45). Destabilization of the earliest resting conformation by AMIGO1 is

457 expected to increase the rate of GxTX–594 dissociation when voltage sensors are partially  
458 activated. To test this prediction, we measured the rate of GxTX–594 dissociation at +30 mV, a  
459 potential at which about 20% of Kv2.1 gating charge is activated with GxTX bound (5). The rate  
460 of GxTX–594 dissociation from Kv2.1 ( $k_{\Delta F}$ ) accelerated from  $0.073 \pm 0.010 \text{ s}^{-1}$  (SEM) in control  
461 cells to  $0.115 \pm 0.015 \text{ s}^{-1}$  (SEM) in cells positive for AMIGO1–YFP fluorescence (Fig. 7). As we  
462 see no evidence that AMIGO1 alters GxTX–594 affinity in cells at rest (Supplemental Fig. 5),  
463 this 1.6-fold acceleration of  $k_{\Delta F}$  is consistent with AMIGO1 destabilizing the earliest resting  
464 conformation of voltage sensors. The thermodynamic model developed to interpret the  $k_{\Delta F}$  of  
465 GxTX–594 dissociation (45) estimates that AMIGO1 decreases the stability of the earliest  
466 resting conformation of each voltage sensor by 1.9-fold or a  $\Delta G_{\text{AMIGO1}}$  of -1.5 kcal/mol for Kv2.1  
467 tetramers (Eqn. L). This result is consistent with AMIGO1 destabilizing the resting voltage  
468 sensor conformation to speed up voltage sensor activation and shift conductance to lower  
469 voltages.

470

471 An extracellular surface potential mechanism of AMIGO1 was not detected

472 To differentiate between mechanisms through which AMIGO1 could change voltage  
473 sensor activation we probed whether the large AMIGO1 extracellular domain is directly  
474 changing the electrostatic environment of Kv2.1's voltage sensors. Per surface charge theory,  
475 local extracellular negative charges could attract positive gating charges to activate channels  
476 (73). AMIGO1 possesses five extracellular glycosylation sites (74), each potentially decorated  
477 with negatively-charged sugar moieties (28). AMIGO1 also has a conserved negatively charged  
478 residue predicted to be near the extracellular side of the membrane (24, 74). Similar structural  
479 characteristics are found in Nav  $\beta$  auxiliary subunits which, like AMIGO1, are glycosylated,  
480 single transmembrane pass protein with an immunoglobulin-domain. Nav  $\beta$ 1 has been proposed  
481 to interact with Nav1.4  $\alpha$  subunit through surface charge effects (75–77). We tested if AMIGO1  
482 likewise affects Kv2.1 activation through electrostatic surface charge interactions.

483 To measure the electrostatics of the environment immediately surrounding the Kv2.1  
484 voltage sensor domain complex with and without AMIGO1, we employed far-red polarity-  
485 sensitive fluorescence (78). The polarity-sensitive fluorophore, JP, was localized to the Kv2.1  
486 voltage sensor by conjugating GxTX to JP at either residue Ser13 or Lys27 (46). When GxTX  
487 binds to the extracellular S3b region of the Kv2.1 channel, Ser13 and Lys27 occupy positions of  
488 distinct polarity (46). At resting membrane potentials, GxTX Ser13Pra(JP) has an emission  
489 maximum of 644 nm, consistent with the homology-based prediction that Ser13 of GxTX  
490 localizes in an aqueous environment branched away from S4. Conversely, GxTX Lys27Pra(JP)  
491 has an emission maximum of 617 nm, consistent with the prediction that Lys27 sits in the polar  
492 region of the membrane adjacent to S4 (46). If AMIGO1 were to alter the electrostatic  
493 environment of the resting conformation of the Kv2.1 voltage sensor domain, we would expect  
494 either of these environmental point detectors, GxTX Ser13Pra(JP) or GxTX Lys27Pra(JP), to  
495 exhibit an altered emission maximum.

496 Full emission spectra of JP fluorescence from Kv2.1–CHO cells transfected with  
497 AMIGO1–YFP and treated with GxTX Ser13Pra(JP) or GxTX Lys27Pra(JP) were fitted with 2-  
498 component split pseudo-Voigt functions (Fig. 8C, F). Fitting shows emission peaks, 644 nm and  
499 617 nm, respectively, are unchanged with or without AMIGO1–YFP, consistent with the local  
500 electrostatic environment surrounding the JP probes positioned on resting Kv2.1 voltage sensors  
501 not being altered by AMIGO1 expression. Previous work has shown that GxTX Lys27Pra(JP)  
502 emission peak wavelength is sensitive to conformational changes among early resting states of

503 voltage sensors (46). The absence of any AMIGO1-induced change in environment for either of  
504 these GxTX sidechains suggests that AMIGO1 does not cause significant changes to the local  
505 environment of the GxTX binding site on the S3b segment of Kv2.1, nor the GxTX position in  
506 the membrane when bound to the channel. These results are consistent with destabilization of the  
507 GxTX binding site by AMIGO1 being indirect, as the binding site itself appears to retain the  
508 same conformation and local environment in the presence of AMIGO1. However, it remains  
509 possible that AMIGO1 acts extracellularly to modulate Kv2.1 by a mechanism that these  
510 GxTX(JP)-based sensors do not detect.

511 We also tested whether AMIGO1 acts by a surface charge mechanism with a classical  
512 charge screening approach. Surface charge interactions can be revealed by increasing the  
513 concentration of  $Mg^{2+}$  to screen, or minimize, the impact of fixed negative charges near the  
514 voltage sensors (73, 79). If AMIGO1 alters surface potential, we would expect elevated  $Mg^{2+}$  to  
515 shrink  $\Delta V_{i, Mid}$ . To determine whether surface charge screening suppresses the AMIGO1 effect,  
516 voltage clamp experiments were conducted as in Fig. 3, except external recording solutions  
517 contained 100 mM  $Mg^{2+}$  (Fig. 9A, B, C). Kv2.1 requires more positive voltage steps to activate  
518 in high  $Mg^{2+}$  solutions (Table 1), consistent with sensitivity to surface charge screening (80). In  
519 high  $Mg^{2+}$ , AMIGO1 effected a  $\Delta V_{i, Mid}$  of  $-7.4 \pm 2.4$  mV (SEM) (Fig. 10H) but did not change  $z_i$   
520 (Fig. 9G) (Table 1). When compared to low  $Mg^{2+}$  conditions by Ordinary 2-way ANOVA,  
521  $\Delta V_{i, Mid}$  was not significantly different in normal versus 100 mM  $Mg^{2+}$  (interaction of  $p = 0.33$ ).  
522 Hence,  $Mg^{2+}$  altered Kv2.1 activation in a manner consistent with surface charge screening, yet  
523  $Mg^{2+}$  did not detectably abrogate the AMIGO1 effect. However, we cannot rule out the  
524 possibility of a screened site that is inaccessible to  $Mg^{2+}$ . While neither extracellular fluorescence  
525 measurements nor surface charge screening detected an extracellular impact of AMIGO1, we are  
526 not able to rule out the possibility of an extracellular coupling to AMIGO1 that was not detected  
527 by these methods.

## 528 Discussion

529 We asked whether AMIGO1 modulates Kv2.1 conductance by modulating conformational  
530 changes of pore opening or voltage sensor activation. We found that AMIGO1 destabilizes the  
531 resting, inward conformation of Kv2.1 voltage sensors, causing channels to activate at more  
532 negative voltages. This conclusion is supported by three major results:  
533

534 1) *AMIGO1 destabilizes the earliest resting conformation of Kv2.1 voltage sensors.*

535 AMIGO1 expression accelerated conductance activation only at a subset of voltages where  
536 the activation kinetics are voltage sensitive (Fig. 3M). When voltage sensor movements were  
537 measured directly, gating current recordings revealed an acceleration of the forward rate constant  
538 ( $\tau_{ON}$ ) of gating charge activation in cells with AMIGO1. Between 0 and 120 mV, pore opening is  
539 10-30x slower than  $I_{g,ON}$  decay (Fig. 3M, 6N), too slow to influence the first few ms of  $I_{g,ON}$ .  
540 When the change in the forward rate  $\alpha_{0mV}$  (Fig. 6N), was used to estimate the amount of energy  
541 AMIGO1 contributes to modulating Kv2.1 conformational bias, we found that AMIGO1  
542 imparted -1.3 kcal/mol per channel (Eqn. J) to  $\Delta G^{\ddagger}_{AMIGO1}$ . From this result we conclude that  
543 AMIGO1 speeds the rate of conformational change between the earliest resting conformation  
544 and its transition state in the activation path. Additionally, the AMIGO1 effect on GxTX-594  
545 dissociation at +30 mV is consistent with AMIGO1 opposing the action of GxTX-594, which  
546 stabilizes resting voltage sensors. All available evidence indicates that AMIGO1 destabilizes the  
547 earliest resting conformation of Kv2.1 voltage sensors. We estimate that AMIGO1 destabilizes  
548 the fully resting conformation of Kv2.1 channels by  $\sim 3$  kcal/mol, relative to the fully active open  
549 state, and that about half of this energy lowers the barrier for the initial exit of voltage sensors  
550 from their resting conformation (Fig. 10A).  
551

552 2) *AMIGO1 has a greater impact on the voltage sensors than the pore opening.*

553 Free energy estimates indicate more AMIGO1 perturbation of the  $Q-V$  than the midpoint of  
554 the  $G-V$ . The  $\Delta G$  for AMIGO1's impact on voltage sensor activation ranged from -1.9 kcal/mol  
555 to -3.1 kcal/mol depending on the calculation method (Table 2). Yet, the  $\Delta G_{AMIGO1}$  calculated at  
556 the conductance midpoint was only -0.3 kcal/mol (Table 1). This lesser impact on pore opening  
557 is consistent with a direct impact of AMIGO1 on voltage sensor movements which are coupled  
558 to pore opening. Notably  $\Delta G_{AMIGO1}$  calculated at the conductance midpoint widens to -0.8  
559 kcal/mol when voltage sensor activation is limited with GxTX-594. When we looked at pore  
560 opening directly, we saw no evidence suggesting a direct effect of AMIGO1. We saw no change  
561 in the slope of the  $G-V$  relationship with AMIGO1 (Table 1), nor sigmoidicity (Fig. 3), nor  
562 single channel measurements (Fig. 4). While these negative results do not eliminate the  
563 possibility that AMIGO1 has a small direct effect on pore opening, these negative results  
564 constrain the effect size of AMIGO1 on pore opening equilibria to be smaller than the error  
565 associated with our measurements.  
566

567 3) *The AMIGO1 impact on conductance is malleable*

568 In Kv2.1-CHO cells, AMIGO1 shifts the  $V_{Mid}$  of conductance by  $-5.7 \pm 2.2$  mV (SEM). With  
569 GxTX-594, the AMIGO1  $G-V$  shift widens to  $-22.3 \pm 4.8$  (SEM) (Table 1). This remarkable  
570 result indicates that the AMIGO1 effect on conductance can change in magnitude. While we  
571 have not completely excluded the possibility that AMIGO1 has a direct interaction with GxTX-

572 594, we think this unlikely, as we saw no sign of an AMIGO1-dependent environmental change  
573 around GxTX–JP conjugates, and GxTX–594 had a similar affinity for resting Kv2.1. We think  
574 it is more likely that AMIGO1 and GxTX–594 interact only allosterically, and favor the  
575 explanation that GxTX makes the  $V_{i, \text{Mid}}$  of conductance more sensitive to the early voltage sensor  
576 transition which AMIGO1 modulates. After its fast voltage sensor movement, Kv2.1 has a slow  
577 conductance-activating step that makes the 4<sup>th</sup> power of the  $Q-V$  not predictive of the  $G-V$  (3–5,  
578 57). GxTX stabilizes the earliest resting conformation of Kv2.1 voltage sensors such that 4<sup>th</sup>  
579 power Boltzmann fits to the  $G-V$  are similar to the  $Q-V$  (5). This suggests the  $V_{i, \text{Mid}}$  is more  
580 responsive to AMIGO1 in GxTX–594 because the  $G-V$  becomes limited by early voltage sensor  
581 movement.

582 To test the idea that AMIGO1 modulation of voltage sensors could result in different  $\Delta V_{i, \text{Mid}}$   
583 of  $G-V$ s, we performed calculations with a voltage sensor shift model composed of simple gating  
584 equations. This voltage sensor shift model incorporates distinct  $V_{1/2}$  values assigned to  
585 independent voltage sensor ( $V_{\text{VSD}, 1/2}$ ) and pore ( $V_{\text{Pore}, 1/2}$ ) transitions, all of which must activate to  
586 allow channel opening. Calculations incorporating a constant  $\Delta V_{\text{VSD}, 1/2}$  shift with no change in  
587  $V_{\text{Pore}, 1/2}$  demonstrate that the  $\Delta V_{i, \text{Mid}}$  of  $G-V$  can be malleable. In these calculations an AMIGO1  
588 shift of  $\Delta V_{\text{VSD}, 1/2} = -22.4$  mV resulted in  $\Delta V_{i, \text{Mid}} = -5.0$  mV (Fig. 10B), similar to the empirical  
589 measurement  $\Delta V_{i, \text{Mid}} = -5.7$  mV of Kv2.1 with AMIGO1 (Fig. 3). However, when  $V_{\text{VSD}, 1/2}$  was  
590 modified to fit GxTX–594 data, this same AMIGO1 shift of  $\Delta V_{\text{VSD}, 1/2} = -22.4$  mV yielded a  
591 larger shift  $G-V$  shift,  $\Delta V_{i, \text{Mid}} = -21.8$  mV (Fig. 10B). While the gating model implied by these  
592 calculations is highly simplified and does not recapitulate all of our data, it does demonstrate a  
593 mechanism by which a fixed modulation of voltage sensors could result in varying  $\Delta V_{i, \text{Mid}}$  shifts.  
594 As the voltage dependence of Kv2.1 activation is dynamically modulated by many forms of  
595 cellular regulation and can vary dramatically (16–20, 81–86), the impact of AMIGO1 might also  
596 fluctuate. A malleable impact of AMIGO1 in response to Kv2.1 regulation could perhaps explain  
597 why a larger  $G-V$  shift was originally reported (22), than was observed here or elsewhere (23).

598 The voltage sensor shift mechanism we propose does not require changes in pore opening, or  
599 voltage sensor-pore coupling. Maverick and colleagues (23) suggested that the effects of  
600 AMIGO proteins on Kv2.1 conductance could be described by increasing the coupling between  
601 the voltage sensor and pore opening without a shift in the  $Q-V$  curve (23), similar to a  
602 mechanism by which leucine-rich-repeat-containing protein 26, LRRC26, modulates large-  
603 conductance  $\text{Ca}^{2+}$ -activated  $\text{K}^{+}$  channels (37). As the precise voltage sensor-pore coupling  
604 mechanisms for Kv2.1 channels have yet to be defined, we cannot rule out the possibility that  
605 AMIGO1 also alters coupling. However, we see no reason that AMIGO1 must do anything other  
606 than destabilize the earliest resting conformation of voltage sensors to modulate Kv2.1  
607 conductance.

608

## 609 Limitations

610 More detailed investigation of the AMIGO1 impact on the Kv2.1 activation pathway was  
611 limited by the relatively small magnitude of AMIGO1-dependent effects versus the cell-to-cell  
612 variability, with  $\Delta V_{i, \text{Mid}}$  as low as 5 mV, and standard deviations for  $V_{i, \text{Mid}}$  of 4 to 9 mV (Table 1,  
613 excluding GxTX–594). While we compensated for the limited power of the AMIGO1 effect by  
614 increasing replicates, a decreased cell-to-cell would enable more precise biophysical  
615 investigation. This degree of cell-to-cell variability does not appear to be unique to our  
616 laboratory. Midpoints reported for rat Kv2.1 activation in HEK293 cells span a 36 mV range,  
617 from -20.2 mV to 16.4 mV (22, 23, 67, 72, 87–95). When we calculated  $V_{\text{Mid}}$  standard deviation

618 values from the standard errors and n-values in these studies, standard deviations ranged from 1  
619 to 17 mV, on par with our own. We suspect these notable  $V_{Mid}$  deviations result from the many  
620 different types of regulation to which Kv2.1 channels are susceptible (20, 21). Techniques to  
621 constrain the cell-to-cell variability in Kv2.1 function could allow more precise mechanistic  
622 studies of AMIGO1 modulation.

623 Our interpretations assume that the AMIGO1 effect is similar whether Kv2.1 is expressed at  
624 low density to measure  $K^+$  currents or at high density for gating current and imaging  
625 experiments. Auxiliary subunit interactions with pore  $\alpha$  subunits can be influenced by many  
626 factors that can alter their assembly and functional impact on channel currents (96–101).  
627 However, if Kv2.1 channels in  $K^+$  current recording were modulated less by AMIGO1, we  
628 would expect a decrease in Boltzmann slope of the fit, a bimodal  $G-V$  relation, or increased cell-  
629 to-cell variability with AMIGO1. We do not observe any of these with CHO cells. The similar  
630 impact of AMIGO1 on Kv2.1 conductance in two cell lines (Table 1) and consistency in effect  
631 magnitudes with an independent report (23), further suggest that AMIGO1 effect is saturating in  
632 our  $K^+$  conductance measurements. Thus, while incomplete complex assembly and other factors  
633 could in theory influence the magnitude of the AMIGO1 impact on Kv2.1 conductance, we do  
634 not see evidence that would negate our biophysical assessment of the mechanism through which  
635 AMIGO1 alters Kv2.1 conductance.

636 The most parsimonious explanation for the effect AMIGO1 has on the Kv2.1 conduction–  
637 voltage relation seems to be a direct interaction with Kv2.1 voltage sensors. However, it also  
638 seems possible that AMIGO1 proteins could change cellular regulation of which in turn  
639 modulates Kv2.1. Even if AMIGO1 acts by an indirect mechanism, our mechanistic conclusions  
640 remain valid, as they are not predicated on a direct protein–protein interaction between AMIGO1  
641 and Kv2.1.

642

#### 643 Potential physiological consequences of an AMIGO1 gating shift

644 The impact of AMIGO1 on Kv2.1 voltage sensors suggests that all voltage-dependent  
645 Kv2 functions are modulated by AMIGO1. How might the AMIGO1 impact on voltage sensor  
646 dynamics affect cellular physiology? As AMIGO1 is colocalized with seemingly all the Kv2  
647 protein in mammalian brain neurons (22, 28, 102), our results suggest that AMIGO1 could cause  
648 Kv2 voltage-dependent functions to occur at more negative potentials in neurons. Consistent  
649 with this suggestion,  $I_K$  currents from hippocampal pyramidal neurons isolated from AMIGO1  
650 knockout mice are altered compared to wild type  $I_K$  currents (25). AMIGO1 knockout mice  
651 display schizophrenia-related features (25) and AMIGO1 knockdown zebrafish have deformed  
652 neural tracts (26). However, it is unclear whether these deficits are due to effects on channel  
653 gating or other functions of AMIGO1, such as extracellular adhesion. In addition to electrical  
654 signaling, Kv2 proteins have important nonconducting functions (28, 67, 103–106), which  
655 AMIGO1 could potentially impact. Currently, we can only speculate about whether  
656 physiological impacts of AMIGO1 are due to alteration of Kv2-mediated signaling.

657 Are the AMIGO1 effects on Kv2.1 conductance activation big enough to meaningfully  
658 impact cellular electrophysiology? To begin to address this question, we estimated the impact  
659 that AMIGO1 would have on neuronal action potentials. In mammalian neurons, Kv2  
660 conductance can speed action potential repolarization (7, 107), dampen the fast  
661 afterdepolarization phase (107), deepen trough voltage, and extend after-hyperpolarization (7) to  
662 impact repetitive firing (7, 107–110). To estimate the impact AMIGO1 might have on the action  
663 potentials, we superimposed the impact of AMIGO1 measured in Kv2.1–CHO cells onto the

664 Kv2 conductance in rat superior cervical ganglion (SCG) neurons, which Liu and Bean (7) found  
665 to account for ~55% of outward current during an action potential. We roughly approximated an  
666 SCG action potential as a 1.5 ms period at 0 mV, during which the parameters fit by Liu and  
667 Bean predict 2.2% of the maximal Kv2 conductance will be activated. If the Kv2 parameters are  
668 modified to mimic removal of AMIGO1, SCG neuron Kv2 conductance at the end of the mock  
669 action potential decreases by 70% (Table 3). This large effect due to small changes in  
670 conductance activation suggests that the AMIGO1 gating shift could have a profound impact on  
671 electrical signaling. Furthermore, we think the AMIGO1 impact could be even greater. Liu and  
672 Bean found that in SCG neurons, Kv2 activation lacks the slow pore-opening step we see in  
673 Kv2.1-CHO cells, and SCG Kv2 kinetics were effectively modeled by a Hodgkin-Huxley  $n^4$   
674 model of activation (111). This suggests that only voltage sensor activation limits conductance  
675 activation in the SCG neurons. When the impact of AMIGO1 on Kv2.1-CHO voltage sensors is  
676 applied to SCG neuron parameters, Kv2 conductance at the end of the mock action potential  
677 decreases by 89% (Table 3). This analysis suggests that removal of the AMIGO1 effect in  
678 neurons could be functionally equivalent to blocking the majority of the Kv2 current during an  
679 action potential, which would in turn be expected to have impacts on repetitive firing (7, 107–  
680 110). However, we stress that any predicted impact of AMIGO1 on action potentials is merely  
681 speculation.

## 682 Conclusions

683 To shift the activation midpoint of Kv2.1 conductance to lower voltages, AMIGO1  
684 destabilizes the earliest resting conformations of Kv2.1 voltage sensors relative to more activated  
685 conformations. While we cannot rule out a direct influence on pore dynamics, we saw no  
686 indication of such. We propose that AMIGO1 shifts the voltage-dependence of Kv2.1  
687 conduction to more negative voltages by modulating early voltage sensor movements.  
688 We also propose that because AMIGO1 acts on early voltage sensor movements, modulation of  
689 Kv2 gating can alter the impact of AMIGO1 on  $K^+$  conductance.

690

## Author Contributions

Rebecka J. Sepela

Conceptualization, Data curation, Formal analysis, Funding acquisition, Investigation, Methodology, Project administration, Visualization, Writing – original draft, Writing – review and editing

Robert G. Stewart

Formal analysis, Visualization

Luis A. Valencia

Formal analysis, Visualization

Parashar Thapa

Resources

Zeming Wang

Resources

Bruce E. Cohen

Conceptualization, Funding acquisition, Project administration, Writing – review and editing

Jon T. Sack

Conceptualization, Funding acquisition, Investigation, Methodology, Project administration, Supervision, Writing – original draft, Writing – review and editing

## Acknowledgements

We thank Vladimir Yarov-Yarovoy, James Trimmer, Karen Zito, and Tsung-Yu Chen of University of California Davis for constructive feedback integral to design and synthesis of experimental ideas. The authors would like to thank the UC Davis statisticians Dr. Sandra Taylor and Dr. Susan Stewart and as well as Karl Brown for their consultation on statistical approaches.

This research was funded by National Institutes of Health grants T32GM007377 (RJS), F31NS108614 (RJS), R01NS096317 (JTS and BEC), and R21EY026449 (JTS). The GxTX-Ser13Cys, GxTX-Ser13Pra, and GxTX-Lys27Pra peptides were synthesized at the Molecular Foundry of the Lawrence Berkeley National Laboratory under U.S. Department of Energy contract DE-AC02-05CH11231. The authors declare no competing financial interests.

## Competing Interests

We declare no competing interests.

## References

1. Kihira, Y., T.O. Hermanstynne, and H. Misonou. 2010. Formation of heteromeric Kv2 channels in mammalian brain neurons. *J. Biol. Chem.* 285:15048–15055.
2. Long, S.B., X. Tao, E.B. Campbell, and R. MacKinnon. 2007. Atomic structure of a voltage-dependent K<sup>+</sup> channel in a lipid membrane-like environment. *Nature.* 450:376–382.
3. Islas, L.D., and F.J. Sigworth. 1999. Voltage sensitivity and gating charge in Shaker and Shab family potassium channels. *J. Gen. Physiol.* 114:723–742.
4. Scholle, A., S. Dugarmaa, T. Zimmer, M. Leonhardt, R. Koopmann, B. Engeland, O. Pongs, and K. Benndorf. 2004. Rate-limiting reactions determining different activation kinetics of Kv1.2 and Kv2.1 channels. *J. Membr. Biol.* 198:103–12.
5. Tilley, D.C., J.M. Angueyra, K.S. Eum, H. Kim, L.H. Chao, A.W. Peng, and J.T. Sack. 2019. The tarantula toxin GxTx detains K<sup>+</sup> channel gating charges in their resting conformation. *J. Gen. Physiol.* 151:292–315.
6. Du, J., L.L. Haak, E. Phillips-Tansey, J.T. Russell, and C.J. McBain. 2000. Frequency-dependent regulation of rat hippocampal somato-dendritic excitability by the K<sup>+</sup> channel subunit Kv2.1. *J. Physiol.* 522 Pt 1:19–31.
7. Liu, P.W., and B.P. Bean. 2014. Kv2 channel regulation of action potential repolarization and firing patterns in superior cervical ganglion neurons and hippocampal CA1 pyramidal neurons. *J. Neurosci.* 34:4991–5002.
8. Malin, S.A., and J.M. Nerbonne. 2002. Delayed rectifier K currents, IK, are encoded by Kv2-subunits and regulate tonic firing in mammalian sympathetic neurons. *Mol. Biol.* 22:10094–10105.
9. Hönigsperger, C., M.J. Nigro, and J.F. Storm. 2017. Physiological roles of Kv2 channels in entorhinal cortex layer II stellate cells revealed by Guangxitoxin-1E. *J. Physiol.* 595:739–757.
10. Romer, S.H., A.S. Deardorff, and R.E.W. Fyffe. 2019. A molecular rheostat: Kv2.1 currents maintain or suppress repetitive firing in motoneurons. *J. Physiol.* 597:3769–3786.
11. Vacher, H., D.P. Mohapatra, and J.S. Trimmer. 2008. Localization and targeting of voltage-dependent ion channels in mammalian central neurons. *Physiol. Rev.* 88:1407–1447.
12. Specca, D.J., G. Ogata, D. Mandikian, H.I. Bishop, S.W. Wiler, K. Eum, H.J. Wenzel, E.T. Doisy, L. Matt, K.L. Campi, M.S. Golub, J.M. Nerbonne, J.W. Hell, B.C. Trainor, J.T. Sack, P.A. Schwartzkroin, and J.S. Trimmer. 2014. Deletion of the Kv2.1 delayed rectifier potassium channel leads to neuronal and behavioral hyperexcitability. *Genes, Brain Behav.* 13:394–408.
13. Kang, S.K., C.G. Vanoye, S.N. Misra, D.M. Echevarria, J.D. Calhoun, J.B. O’Connor, K.L. Fabre, D. McKnight, L. Demmer, P. Goldenberg, L.E. Grote, I. Thiffault, C. Saunders, K.A. Strauss, A. Torkamani, J. van der Smagt, K. van Gassen, R.P. Carson, J. Diaz, E. Leon, J.E. Jacher, M.C. Hannibal, J. Litwin, N.R. Friedman, A. Schreiber, B. Lynch, A. Poduri, E.D. Marsh, E.M. Goldberg, J.J. Millichap, A.L.J. George, and J.A. Kearney. 2019. Spectrum of K(v) 2.1 dysfunction in KCNB1-associated neurodevelopmental disorders. *Ann. Neurol.* 86:899–912.
14. Torkamani, A., K. Bersell, B.S. Jorge, R.L. Bjork, J.R. Friedman, C.S. Bloss, J. Cohen, S. Gupta, S. Naidu, C.G. Vanoye, A.L. George, and J.A. Kearney. 2014. De novo KCNB1 mutations in epileptic encephalopathy. *Ann. Neurol.* 76:529–540.
15. Thiffault, I., D.J. Specca, D.C. Austin, M.M. Cobb, K.S. Eum, N.P. Safina, L. Grote, E.G. Farrow, N. Miller, S. Soden, S.F. Kingsmore, J.S. Trimmer, C.J. Saunders, and J.T. Sack. 2015. A novel epileptic encephalopathy mutation in KCNB1 disrupts Kv2.1 ion selectivity, expression, and localization. *J. Gen. Physiol.* 146:399–410.
16. Misonou, H., M. Menegola, D.P. Mohapatra, L.K. Guy, K.-S. Park, and J.S. Trimmer. 2006. Bidirectional activity-dependent regulation of neuronal ion channel phosphorylation. *J. Neurosci.* 26:13505–13514.
17. Misonou, H., D.P. Mohapatra, M. Menegola, and J.S. Trimmer. 2005. Calcium- and metabolic state-dependent modulation of the voltage-dependent Kv2.1 channel regulates neuronal excitability in response to ischemia. *J. Neurosci.* 25:11184–11193.
18. Aras, M.A., R.A. Saadi, and E. Aizenman. 2009. Zn<sup>2+</sup> regulates Kv2.1 voltage-dependent gating and localization following ischemia. *Eur. J. Neurosci.* 30:2250–2257.
19. Misonou, H., S.M. Thompson, and X. Cai. 2008. Dynamic regulation of the Kv2.1 voltage-gated potassium channel during brain ischemia through neuroglial interaction. *J. Neurosci.* 28:8529–38.
20. Murakoshi, H., G. Shi, R.H. Scannevin, and J.S. Trimmer. 1997. Phosphorylation of the Kv2.1 K<sup>+</sup> channel alters voltage-dependent activation. *Mol. Pharmacol.* 52:821–8.

21. Plant, L.D., E.J. Dowdell, I.S. Dementieva, J.D. Marks, and S.A.N. Goldstein. 2011. SUMO modification of cell surface Kv2.1 potassium channels regulates the activity of rat hippocampal neurons. *J. Gen. Physiol.* 137:441–54.
22. Peltola, M.A., J. Kuja-Panula, S.E. Lauri, T. Taira, and H. Rauvala. 2011. AMIGO is an auxiliary subunit of the Kv2.1 potassium channel. *EMBO Rep.* 12:1293–1299.
23. Maverick, E.E., A.N. Leek, and M.M. Tamkun. 2021. Kv2 channel/AMIGO  $\beta$ -subunit assembly modulates both channel function and cell adhesion molecule surface trafficking. *J. Cell Sci.*
24. Kuja-Panula, J., M. Kiiltomäki, T. Yamashiro, A. Rouhiainen, and H. Rauvala. 2003. AMIGO, a transmembrane protein implicated in axon tract development, defines a novel protein family with leucine-rich repeats. *J. Cell Biol.* 160:963–973.
25. Peltola, M.A., J. Kuja-Panula, J. Liuhanen, V. Vöikar, P. Piepponen, T. Hiekkalinna, T. Taira, S.E. Lauri, J. Suvisaari, N. Kuleskaya, T. Paunio, and H. Rauvala. 2015. AMIGO-Kv2.1 potassium channel complex is associated with schizophrenia-related phenotypes. *Schizophr. Bull.* 42:105.
26. Zhao, X., J. Kuja-Panula, M. Sundvik, Y.-C. Chen, V. Aho, M.A. Peltola, T. Porkka-Heiskanen, P. Panula, and H. Rauvala. 2014. Amigo adhesion protein regulates development of neural circuits in zebrafish brain. *J. Biol. Chem.* 289:19958–19975.
27. Chen, Y., H.H. Hor, and B.L. Tang. 2012. AMIGO is expressed in multiple brain cell types and may regulate dendritic growth and neuronal survival. *J. Cell. Physiol.* 227:2217–2229.
28. Bishop, H.I., M.M. Cobb, M. Kirmiz, L.K. Parajuli, D. Mandikian, A.M. Philp, M. Melnik, J. Kuja-Panula, H. Rauvala, R. Shigemoto, K.D. Murray, and J.S. Trimmer. 2018. Kv2 ion channels determine the expression and localization of the associated AMIGO-1 cell adhesion molecule in adult brain neurons. *Front. Mol. Neurosci.* 11.
29. Cregg, R., B. Laguda, R. Werdehausen, J.J. Cox, J.E. Linley, J.D. Ramirez, I. Bodi, M. Markiewicz, K.J. Howell, Y.C. Chen, K. Agnew, H. Houlden, M.P. Lunn, D.L.H. Bennett, J.N. Wood, and M. Kinali. 2013. Novel mutations mapping to the fourth sodium channel domain of nav1.7 result in variable clinical manifestations of primary erythromelalgia. *NeuroMolecular Med.* 15:265–278.
30. Huang, J., M. Estacion, P. Zhao, F.B. Dib-Hajj, B. Schulman, A. Abicht, I. Kurth, K. Brockmann, S.G. Waxman, and S.D. Dib-Hajj. 2019. A novel gain-of-function Nav1.9 mutation in a child with episodic pain. *Front. Neurosci.* 13:1–11.
31. Abriel, H., C. Cabo, X.H.T. Wehrens, I. Rivolta, H.K. Motoike, M. Memmi, C. Napolitano, S.G. Priori, and R.S. Kass. 2001. Novel arrhythmogenic mechanism revealed by a long-QT syndrome mutation in the cardiac Na<sup>+</sup> channel. *Circ. Res.* 88:740–745.
32. Dudem, S., R.J. Large, S. Kulkarni, H. McClafferty, I.G. Tikhonova, G.P. Sergeant, K.D. Thornbury, M.J. Shipston, B.A. Perrino, and M.A. Hollywood. 2020. LINGO1 is a regulatory subunit of large conductance, Ca<sup>2+</sup>-activated potassium channels. *Proc. Natl. Acad. Sci. U. S. A.* 117:2194–2200.
33. Rockman, M.E., A.G. Vouga, and B.S. Rothberg. 2020. Molecular mechanism of BK channel activation by the smooth muscle relaxant NS11021. *J. Gen. Physiol.* 152.
34. Horrigan, F.T., and R.W. Aldrich. 2002. Coupling between voltage sensor activation, Ca<sup>2+</sup> binding and channel opening in large conductance (BK) potassium channels. *J. Gen. Physiol.* 120:267–305.
35. Zhu, W., T.L. Voelker, Z. Varga, A.R. Schubert, J.M. Nerbonne, and J.R. Silva. 2017. Mechanisms of noncovalent  $\beta$  subunit regulation of NaV channel gating. *J. Gen. Physiol.* 149:813–831.
36. Barro-Soria, R., M.E. Perez, and H.P. Larsson. 2015. KCNE3 acts by promoting voltage sensor activation in KCNQ1. *Proc. Natl. Acad. Sci. U. S. A.* 112:E7286–E7292.
37. Yan, J., and R.W. Aldrich. 2010. LRRC26 auxiliary protein allows BK channel activation at resting voltage without calcium. *Nature.* 466:513–516.
38. Barro-Soria, R., R. Ramentol, S.I. Liin, M.E. Perez, R.S. Kass, and H.P. Larsson. 2017. KCNE1 and KCNE3 modulate KCNQ1 channels by affecting different gating transitions. *Proc. Natl. Acad. Sci. U. S. A.* 114:E7367–E7376.
39. Nakajo, K., and Y. Kubo. 2015. KCNQ1 channel modulation by KCNE proteins via the voltage-sensing domain. *J. Physiol.* 593:2617–2625.
40. Zhang, J., and J. Yan. 2014. Regulation of BK channels by auxiliary  $\gamma$  subunits. *Front. Physiol.* 5:401.
41. Brackenbury, W.J., and L.L. Isom. 2011. Na<sup>+</sup> channel  $\beta$  subunits: Overachievers of the ion channel family. *Front. Pharmacol.* 2:1–11.
42. Chen, Y., S. Aulia, L. Li, and B.L. Tang. 2006. AMIGO and friends: An emerging family of brain-enriched, neuronal growth modulating, type I transmembrane proteins with leucine-rich repeats (LRR) and cell adhesion molecule motifs. *Brain Res. Rev.* 51:265–274.

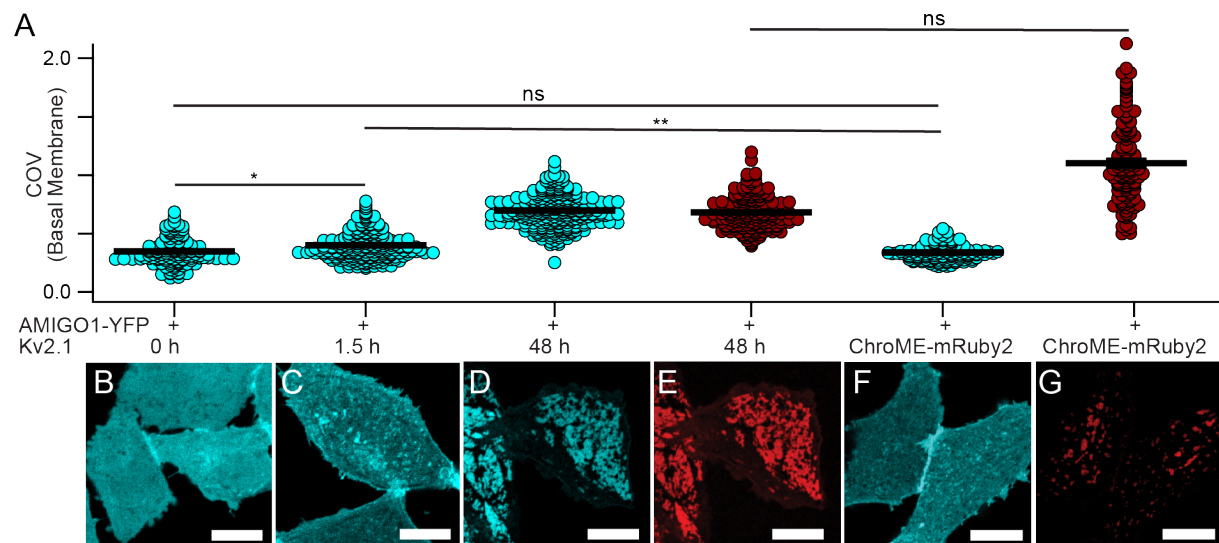
43. Sun, J., and R. MacKinnon. 2020. Structural Basis of Human KCNQ1 Modulation and Gating. *Cell*. 180:340-347.e9.
44. Shen, H., D. Liu, K. Wu, J. Lei, and N. Yan. 2019. Structures of human Nav1.7 channel in complex with auxiliary subunits and animal toxins. *Science*. 1308:1303–1308.
45. Thapa, P., R. Stewart, R.J. Sepela, O. Vivas, L.K. Parajuli, M. Lillya, S. Fletcher-taylor, B.E. Cohen, K. Zito, and J.T. Sack. 2021. EVAP: A two-photon imaging tool to study conformational changes in endogenous Kv2 channels in live tissues. *J. Gen. Physiol.* 153:1–24.
46. Fletcher-Taylor, S., P. Thapa, R.J. Sepela, R. Kaakati, V. Yarov-Yarovoy, J.T. Sack, and B.E. Cohen. 2020. Distinguishing potassium channel resting state conformations in live cells with environment-sensitive fluorescence. *Am. Chem. Soc. Chem. Neurosci.* 11.
47. Tilley, D.C., K.S. Eum, S. Fletcher-Taylor, D.C. Austin, C. Dupre, L.A. Patron, R.L. Garcia, K. Lam, V. Yarov-Yarovoy, B.E. Cohen, and J.T. Sack. 2014. Chemoselective tarantula toxins report voltage activation of wild-type ion channels in live cells. *Proc. Natl. Acad. Sci. U. S. A.* 111:E4789–E4796.
48. Stewart, R., B.E. Cohen, and J.T. Sack. 2021. Fluorescent toxins as ion channel activity sensors. *Methods Enzymol.* 1–24.
49. Trapani, J.G., and S.J. Korn. 2003. Control of ion channel expression for patch clamp recordings using an inducible expression system in mammalian cell lines. *BMC Neurosci.* 4.
50. Liu, X., S.N. Constantinescu, Y. Sun, J.S. Bogan, D. Hirsch, R.A. Weinberg, and H.F. Lodish. 2000. Generation of mammalian cells stably expressing multiple genes at predetermined levels. *Anal. Biochem.* 280:20–28.
51. Mardinly, A.R., I.A. Oldenburg, N.C. Pégard, S. Sridharan, E.H. Lyall, K. Chesnov, S.G. Brohawn, L. Waller, and H. Adesnik. 2018. Precise multimodal optical control of neural ensemble activity. *Nat. Neurosci.* 21:881–893.
52. Lim, S.T., D.E. Antonucci, R.H. Scannevin, and J.S. Trimmer. 2000. A novel targeting signal for proximal clustering of the Kv2.1 K<sup>+</sup> channel in hippocampal neurons. *Neuron*. 25:385–397.
53. Yu, S.P., and G.A. Kerchner. 1998. Endogenous voltage-gated potassium channels in human embryonic kidney (HEK293) cells. *J. Neurosci. Res.* 52:612–7.
54. Sack, J.T., and R.W. Aldrich. 2006. Binding of a gating modifier toxin induces intersubunit cooperativity early in the Shaker K channel’s activation pathway. *J. Gen. Physiol.* 128:119–132.
55. Schoppa, N.E., and F.J. Sigworth. 1998. Activation of Shaker potassium channels. I. Characterization of voltage-dependent transitions. *J. Gen. Physiol.* 111:271–294.
56. Lopatin, A.N., E.N. Makhina, and C.G. Nichols. 1994. Potassium channel block by cytoplasmic polyamines as the mechanism of intrinsic rectification. *Nature*. 372:366–369.
57. Jara-Oseguera, A., I.G. Ishida, G.E. Rangel-Yescas, N. Espinosa-Jalapa, J.A. Pérez-Guzmán, D. Elías-Viñas, R. Le Lagadec, T. Rosenbaum, and L.D. Islas. 2011. Uncoupling charge movement from channel opening in voltage-gated potassium channels by ruthenium complexes. *J. Biol. Chem.* 286:16414–16425.
58. Chowdhury, S., and B. Chanda. 2012. Estimating the voltage-dependent free energy change of ion channels using the median voltage for activation. *J. Gen. Physiol.* 139:3–17.
59. Schindelin, J., I. Arganda-Carreras, E. Frise, V. Kaynig, M. Longair, T. Pietzsch, S. Preibisch, C. Rueden, S. Saalfeld, B. Schmid, J.-Y. Tinevez, D.J. White, V. Hartenstein, K. Eliceiri, P. Tomancak, and A. Cardona. 2012. Fiji: An open-source platform for biological-image analysis. *Nat. Methods*. 9:676–682.
60. Ponce, A., A. Castillo, L. Hinojosa, J. Martinez-Rendon, and M. Cerejido. 2018. The expression of endogenous voltage-gated potassium channels in HEK293 cells is affected by culture conditions. *Physiol. Rep.* 6:e13663.
61. Gamper, N., J.D. Stockand, and M.S. Shapiro. 2005. The use of Chinese hamster ovary (CHO) cells in the study of ion channels. *J. Pharmacol. Toxicol. Methods.* 51:177–185.
62. Isom, L., K. De Jongh, D. Patton, B. Reber, J. Offord, H. Charbonneau, K. Walsh, A. Goldin, and W. Catterall. 1992. Primary structure and functional expression of the beta 1 subunit of the rat brain sodium channel. *Science*. 256:839–842.
63. Isom, L.L., D.S. Ragsdale, K.S. De Jongh, R.E. Westenbroek, B.F.X. Reber, T. Scheuer, and W.A. Catterall. 1995. Structure and function of the  $\beta$ 2 subunit of brain sodium channels, a transmembrane glycoprotein with a CAM motif. *Cell*. 83:433–442.
64. McEwen, D.P., and L.L. Isom. 2004. Heterophilic interactions of sodium channel beta1 subunits with axonal and glial cell adhesion molecules. *J. Biol. Chem.* 279:52744–52752.
65. Kazarinova-Noyes, K., J.D. Malhotra, D.P. McEwen, L.N. Mattei, E.O. Berglund, B. Ranscht, S.R. Levinson, M. Schachner, P. Shrager, L.L. Isom, and Z.C. Xiao. 2001. Contactin associates with Na<sup>+</sup>

- channels and increases their functional expression. *J. Neurosci.* 21:7517–7525.
66. Patino, G.A., L.R.F. Claes, L.F. Lopez-Santiago, E.A. Slat, R.S.R. Dondeti, C. Chen, H.A. O'Malley, C.B.B. Gray, H. Miyazaki, N. Nukina, F. Oyama, P. De Jonghe, and L.L. Isom. 2009. A functional null mutation of SCN1B in a patient with Dravet syndrome. *J. Neurosci.* 29:10764–10778.
67. Kirmiz, M., S. Palacio, P. Thapa, A.N. King, J.T. Sack, and J.S. Trimmer. 2018. Remodeling neuronal ER–PM junctions is a conserved nonconducting function of Kv2 plasma membrane ion channels. *Mol. Biol. Cell.* 29:2410–2432.
68. Manders, E.M.M., J. Stap, G.J. Brakenhoff, R. Van Driel, and J.A. Aten. 1992. Dynamics of three-dimensional replication patterns during the S-phase, analysed by double labelling of DNA and confocal microscopy. *J. Cell Sci.* 103:857–862.
69. Gilchrist, J., S. Das, F. Van Petegem, and F. Bosmans. 2013. Crystallographic insights into sodium-channel modulation by the  $\beta 4$  subunit. *Proc. Natl. Acad. Sci. U. S. A.* 110.
70. Dunn, K.W., M.M. Kamocka, and J.H. McDonald. 2011. A practical guide to evaluating colocalization in biological microscopy. *Am. J. Physiol. Cell Physiol.* 300:C723–742.
71. Cobb, M.M., D.C. Austin, J.T. Sack, and J.S. Trimmer. 2016. Cell cycle-dependent changes in localization and phosphorylation of the plasma membrane Kv2.1 K<sup>+</sup> channel impact endoplasmic reticulum membrane contact sites in COS-1 cells. *J. Biol. Chem.* 291:5527.
72. Milescu, M., F. Bosmans, S. Lee, A.A. Alabi, J. Il Kim, and K.J. Swartz. 2009. Interactions between lipids and voltage sensor paddles detected with tarantula toxins. *Nat. Struct. Mol. Biol.* 16:1080–1085.
73. Green, W.N., and O.S. Andersen. 1991. Surface charges and ion channel function. *Annu. Rev. Physiol.* 53:341–359.
74. Kajander, T., J. Kuja-Panula, H. Rauvala, and A. Goldman. 2011. Crystal structure and role of glycans and dimerization in folding of neuronal leucine-rich repeat protein AMIGO-1. *J. Membr. Biol.* 413:1001–1015.
75. Ednie, A.R., and E.S. Bennett. 2012. Modulation of voltage-gated ion channels by sialylation. *Compr. Physiol.* 2:1269–1301.
76. Ferrera, L., and O. Moran. 2006.  $\beta 1$ -subunit modulates the Nav1.4 sodium channel by changing the surface charge. *Exp. Brain Res.* 172:139–150.
77. Johnson, D., M.L. Montpetit, P.J. Stocker, and E.S. Bennett. 2004. The sialic acid component of the  $\beta 1$  subunit modulates voltage-gated sodium channel function. *J. Biol. Chem.* 279:44303–44310.
78. Cohen, B.E., A. Pralle, X. Yao, G. Swaminath, C.S. Gandhi, Y.N. Jan, B.K. Kobilka, E.Y. Isacoff, and L.Y. Jan. 2005. A fluorescent probe designed for studying protein conformational change. *Proc. Natl. Acad. Sci. U. S. A.* 102:965–970.
79. Elinder, F., and P. Århem. 2003. Metal ion effects on ion channel gating. *Q. Rev. Biophys.* 36:373–427.
80. Broomand, A., F. Österberg, T. Wardi, and F. Elinder. 2007. Electrostatic domino effect in the Shaker K channel turret. *Biophys. J.* 93:2307–2314.
81. Ikematsu, N., M.L. Dallas, F.A. Ross, R.W. Lewis, J.N. Rafferty, J.A. David, R. Suman, C. Peers, D.G. Hardie, and A.M. Evansc. 2011. Phosphorylation of the voltage-gated potassium channel Kv2.1 by AMP-activated protein kinase regulates membrane excitability. *Proc. Natl. Acad. Sci. U. S. A.* 108:18132–18137.
82. Baver, S.B., and K.M.S. O'Connell. 2012. The C-terminus of neuronal Kv2.1 channels is required for channel localization and targeting but not for NMDA-receptor-mediated regulation of channel function. *Neuroscience.* 217:56–66.
83. Mulholland, P.J., E.P. Carpenter-Hyland, M.C. Hearing, H.C. Becker, J.J. Woodward, and L.J. Chandler. 2008. Glutamate transporters regulate extrasynaptic NMDA receptor modulation of Kv2.1 potassium channels. *J. Neurosci.* 28:8801–8809.
84. Misonou, H., D.P. Mohapatra, E.W. Park, V. Leung, D. Zhen, K. Misonou, A.E. Anderson, and J.S. Trimmer. 2004. Regulation of ion channel localization and phosphorylation by neuronal activity. *Nat. Neurosci.* 7:711–718.
85. Cerda, O., and J.S. Trimmer. 2011. Activity-dependent phosphorylation of neuronal Kv2.1 potassium channels by CDK5. *J. Biol. Chem.* 286:28738–28748.
86. Bar, C., M. Kuchenbuch, G. Barcia, A. Schneider, M. Jennesson, G. Le Guyader, G. Lesca, C. Mignot, M. Montomoli, E. Parrini, H. Isnard, A. Rolland, B. Keren, A. Afenjar, N. Dorison, L.G. Sadleir, D. Breuillard, R. Levy, M. Rio, S. Dupont, S. Negrin, A. Danieli, E. Scalais, A. De Saint Martin, S. El Chehadeh, J. Chelly, A. Poisson, A.-S. Lebre, A. Nica, S. Odent, T. Sekhara, V. Brankovic, A. Goldenberg, P. Vrielynck, D. Lederer, H. Maurey, G. Terrone, C. Besmond, L. Hubert, P. Berquin, T. Billette de Villemeur, B. Isidor, J.L. Freeman, H.C. Mefford, C.T. Myers, K.B. Howell, A. Rodríguez-Sacristán Cascajo, P. Meyer, D. Genevieve, A. Guët, D. Doummar, J. Durigneux, M.F. van Dooren, M.C.Y. de Wit, M. Gerard, I. Marey, A.

- Munnich, R. Guerrini, I.E. Scheffer, E. Kabashi, and R. Nabbut. 2020. Developmental and epilepsy spectrum of KCNB1 encephalopathy with long-term outcome. *Epilepsia*. 61:2461–2473.
87. Park, K.-S., D.P. Mohapatra, H. Misonou, and J.S. Trimmer. 2006. Graded regulation of the Kv2.1 potassium channel by variable phosphorylation. *Science*. 313:976–979.
88. Aréchiga-Figueroa, I.A., M. Delgado-Ramírez, R. Morán-Zendejas, and A.A. Rodríguez-Menchaca. 2015. Modulation of Kv2.1 channels inactivation by curcumin. *Pharmacol. Reports*. 67:1273–1279.
89. Delgado-Ramírez, M., J.J. De Jesús-Pérez, I.A. Aréchiga-Figueroa, J. Arreola, S.K. Adney, C.A. Villalba-Galea, D.E. Logothetis, and A.A. Rodríguez-Menchaca. 2018. Regulation of Kv2.1 channel inactivation by phosphatidylinositol 4,5-bisphosphate. *Sci. Rep.* 8:1769.
90. Aréchiga-Figueroa, I.A., R. Morán-Zendejas, M. Delgado-Ramírez, and A.A. Rodríguez-Menchaca. 2017. Phytochemicals genistein and capsaicin modulate Kv2.1 channel gating. *Pharmacol. Reports*. 69:1145–1153.
91. Liu, R., G. Yang, M.-H. Zhou, Y. He, Y.-A. Mei, and Y. Ding. 2016. Flotillin-1 downregulates K(+) current by directly coupling with Kv2.1 subunit. *Protein Cell*. 7:455–60.
92. David, J.-P., J.I. Stas, N. Schmitt, and E. Bocksteins. 2015. Auxiliary KCNE subunits modulate both homotetrameric Kv2.1 and heterotetrameric Kv2.1/Kv6.4 channels. *Sci. Rep.* 5:12813.
93. Li, X.-T., X.-Q. Li, X.-M. Hu, and X.-Y. Qiu. 2015. The inhibitory effects of Ca<sup>2+</sup> channel blocker nifedipine on rat Kv2.1 potassium channels. *PLoS One*. 10:e0124602.
94. Liu, X., Y. Fu, H. Yang, T. Mavlyutov, J. Li, C.R. McCurdy, L.-W. Guo, and B.R. Pattnaik. 2017. Potential independent action of sigma receptor ligands through inhibition of the Kv2.1 channel. *Oncotarget*. 8:59345–59358.
95. O’Connell, K.M.S., R. Loftus, and M.M. Tamkun. 2010. Localization-dependent activity of the Kv2.1 delayed-rectifier K<sup>+</sup> channel. *Proc. Natl. Acad. Sci. U. S. A.* 107:12351–12356.
96. Laedermann, C.J., N. Syam, M. Pertin, I. Decosterd, and H. Abriel. 2013.  $\beta$ 1- and  $\beta$ 3- voltage-gated sodium channel subunits modulate cell surface expression and glycosylation of Nav1.7 in HEK293 cells. *Front. Cell. Neurosci.* 7:137.
97. Eichel, C.A., E.B. Ríos-Pérez, F. Liu, M.B. Jameson, D.K. Jones, J.J. Knickelbine, and G.A. Robertson. 2019. A microtranslatome coordinately regulates sodium and potassium currents in the human heart. *Elife*. 8.
98. Nagaya, N., and D.M. Papazian. 1997. Potassium channel alpha and beta subunits assemble in the endoplasmic reticulum. *J. Biol. Chem.* 272:3022–3027.
99. Gonzalez-Perez, V., X.-M. Xia, and C.J. Lingle. 2014. Functional regulation of BK potassium channels by  $\gamma$ 1 auxiliary subunits. *Proc. Natl. Acad. Sci. U. S. A.* 111:4868–4873.
100. Gonzalez-Perez, V., M. Ben Johny, X.M. Xia, and C.J. Lingle. 2018. Regulatory  $\gamma$ 1 subunits defy symmetry in functional modulation of BK channels. *Proc. Natl. Acad. Sci. U. S. A.* 115:9923–9928.
101. Wang, Y.W., J.P. Ding, X.M. Xia, and C.J. Lingle. 2002. Consequences of the stoichiometry of Slo1,  $\alpha$  and auxiliary  $\beta$  subunits on functional properties of large-conductance Ca<sup>2+</sup>-activated K<sup>+</sup> channels. *J. Neurosci.* 22:1550–1561.
102. Mandikian, D., E. Bocksteins, L.K. Parajuli, H.I. Bishop, O. Cerda, R. Shigemoto, and J.S. Trimmer. 2014. Cell type-specific spatial and functional coupling between mammalian brain Kv2.1 K<sup>+</sup> channels and ryanodine receptors. *J. Comp. Neurol.* 522:3555–3574.
103. Fox, P.D., R.J. Loftus, and M.M. Tamkun. 2013. Regulation of Kv2.1 K(+) conductance by cell surface channel density. *J. Neurosci.* 33:1259–70.
104. Kirmiz, M., N.C. Vierra, S. Palacio, and J.S. Trimmer. 2018. Identification of VAPA and VAPB as Kv2 channel-interacting proteins defining endoplasmic reticulum–plasma membrane junctions in mammalian brain neurons. *J. Neurosci.* 38:7562–7584.
105. Vierra, N.C., M. Kirmiz, D. van der List, L.F. Santana, and J.S. Trimmer. 2019. Kv2.1 mediates spatial and functional coupling of L-type calcium channels and ryanodine receptors in mammalian neurons. *Elife*. 8.
106. Johnson, B., A.N. Leek, L. Solé, E.E. Maverick, T.P. Levine, and M.M. Tamkun. 2018. Kv2 potassium channels form endoplasmic reticulum/plasma membrane junctions via interaction with VAPA and VAPB. *Proc. Natl. Acad. Sci. U. S. A.* 115:E7331 LP-E7340.
107. Newkirk, G.S., D. Guan, N. Dembrow, W.E. Armstrong, and R.C. Foehring. 2021. Kv2 . 1 Potassium Channels Regulate Repetitive Burst Firing in Extratelencephalic Neocortical Pyramidal Neurons. 1–22.
108. Bishop, H.I., D. Guan, E. Bocksteins, L.K. Parajuli, K.D. Murray, M.M. Cobb, H. Misonou, K. Zito, R.C. Foehring, and J.S. Trimmer. 2015. Distinct cell- and layer-specific expression patterns and independent regulation of Kv2 channel subtypes in cortical pyramidal neurons. *J. Neurosci.* 35:14922–14942.

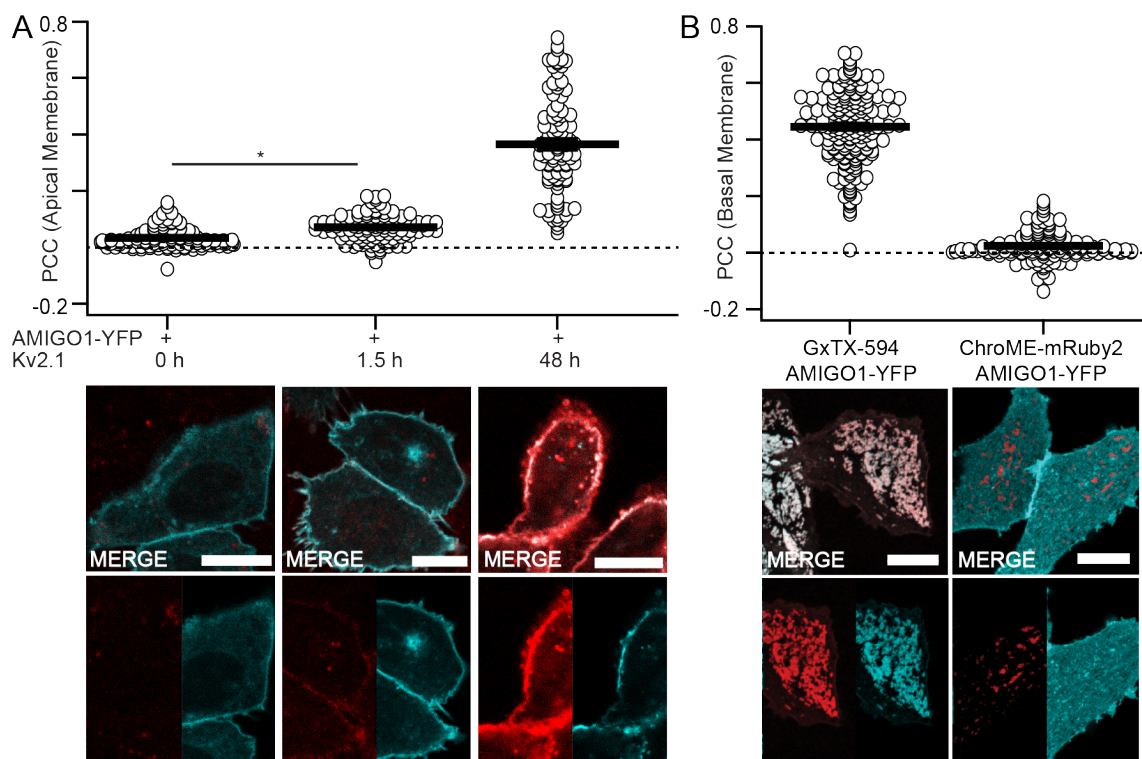
109. Murakoshi, H., and J.S. Trimmer. 1999. Identification of the Kv2.1 K<sup>+</sup> channel as a major component of the delayed rectifier K<sup>+</sup> current in rat hippocampal neurons. *J. Neurosci.* 19:1728–1735.
110. Guan, D., W.E. Armstrong, and R.C. Foehring. 2013. Kv2 channels regulate firing rate in pyramidal neurons from rat sensorimotor cortex. *J. Physiol.* 591:4807–25.
111. Hodgkin, A.L., and A.F. Huxley. 1952. A quantitative description of membrane current and its application to conduction and excitation in nerve. *J Physiol.* 117:500–544.

691



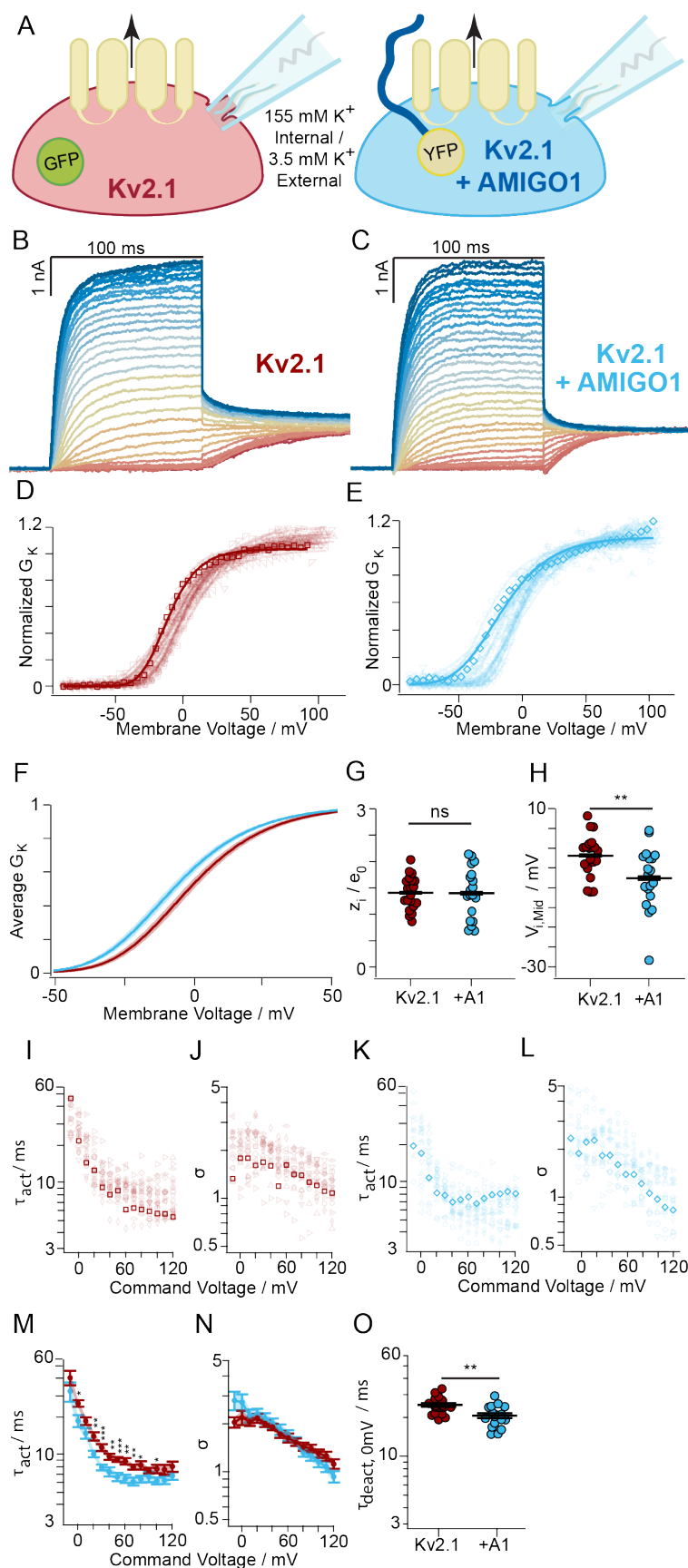
**Figure 1. Kv2.1 reorganizes AMIGO1 in CHO cells.**

(A) Coefficient of variation of fluorescence from AMIGO1–YFP (blue circles), GxTX–594 (red circles), or ChroME–mRuby2 (red circles). Bars are mean  $\pm$  SEM. COV measurements were calculated from confocal images acquired from the glass–adhered basal membrane of the cell (exemplar confocal images in B–G). All cells were transfected with AMIGO1–YFP 48 h prior to imaging. COV from individual cells ( $n$ ) were pooled from 4 separate transfections for each experimental condition. AMIGO1–YFP fluorescence from cells (B) not induced for Kv2.1 expression ( $COV_{0h} = 0.3492 \pm 0.0098$ ,  $n = 134$ ), (C) induced 1.5 h ( $COV_{1.5h} = 0.4013 \pm 0.0077$ ,  $n = 217$ ), (D) induced 48 h ( $COV_{48h} = 0.6984 \pm 0.0083$ ,  $n = 277$ ). (E) GxTX–594 labeling from panel D ( $COV_{48h(GxTX-594)} = 0.6822 \pm 0.010$ ,  $n = 197$ ). (F) AMIGO1–YFP fluorescence from CHO cells which lack Kv2.1 co-transfected with ChroME–mRuby2 ( $COV_{lack} = 0.3377 \pm 0.0059$ ,  $n = 125$ ). (G) ChroME–mRuby2 fluorescence from panel F ( $COV_{(ChroME-mRuby2)} = 1.102 \pm 0.030$ ,  $n = 128$ ). Scale bars 10  $\mu$ m. (Statistics) Outliers removed using ROUT, Q = 1%. Ordinary one-way ANOVA with multiple comparisons. P-values:  $COV_{0h}COV_{1.5h}$ :  $p = 0.0467$ ;  $COV_{0h}COV_{lack}$ :  $p = 0.9936$ ;  $COV_{1.5h}COV_{lack}$ :  $p = 0.0081$ ;  $COV_{48h(GxTX-594)} COV_{(ChroME-mRuby2)}$ :  $p = 0.9010$ . All other p-values  $\leq 0.0001$ .



*Figure 2. AMIGO1 colocalizes with Kv2.1 in CHO cells.*

(A) Costes thresholded, Pearson's colocalization between AMIGO1-YFP and GxTX-594 at cell membrane following, from left to right, 0, 1.5, or 48 h of Kv2.1 induction (exemplar confocal images in B-J below). Mean  $\pm$  SEM (one-tailed  $\geq 0$  t-test):  $PCC_{0h} = 0.0321 \pm 0.0033$ , ( $p < 0.0001$ ),  $n = 101$ ;  $PCC_{1.5h} = 0.0718 \pm 0.0042$ , ( $p < 0.0001$ ),  $n = 118$ ; and  $PCC_{48h} = 0.365 \pm 0.017$ , ( $p < 0.0001$ ),  $n = 101$ . (B) Costes thresholded, Pearson's colocalization between (left to right) AMIGO1-YFP/GxTX-594 and AMIGO1-YFP/ChroME-mRuby2 at the glass-adhered basal membrane of the cell. Exemplar images are the same as in Fig. 1 D-G. From left to right:  $PCC_{GxTX-594} = 0.4449 \pm 0.0090$ , ( $p < 0.0001$ ),  $n = 195$ ;  $PCC_{ChroME-mRuby2} = 0.0242 \pm 0.0045$ , ( $p < 0.0001$ ),  $n = 129$ . Image panels with merge overlays (white) of GxTX-594 (red) and AMIGO1-YFP (cyan) correspond to conditions above. All scale bars are  $10 \mu m$ . (Statistics) Outliers were removed using ROUT,  $Q = 1\%$ . Ordinary one-way ANOVA with multiple comparisons. P-values:  $PCC_{0h}PCC_{1.5h}$ :  $p = 0.346$ ;  $PCC_{1.5h}PCC_{ChroME-mRuby2}$ :  $p = 0.0025$ ;  $PCC_{0h}PCC_{ChroME-mRuby2}$ :  $p = 0.9777$ . All other p-values were  $\leq 0.0001$ .



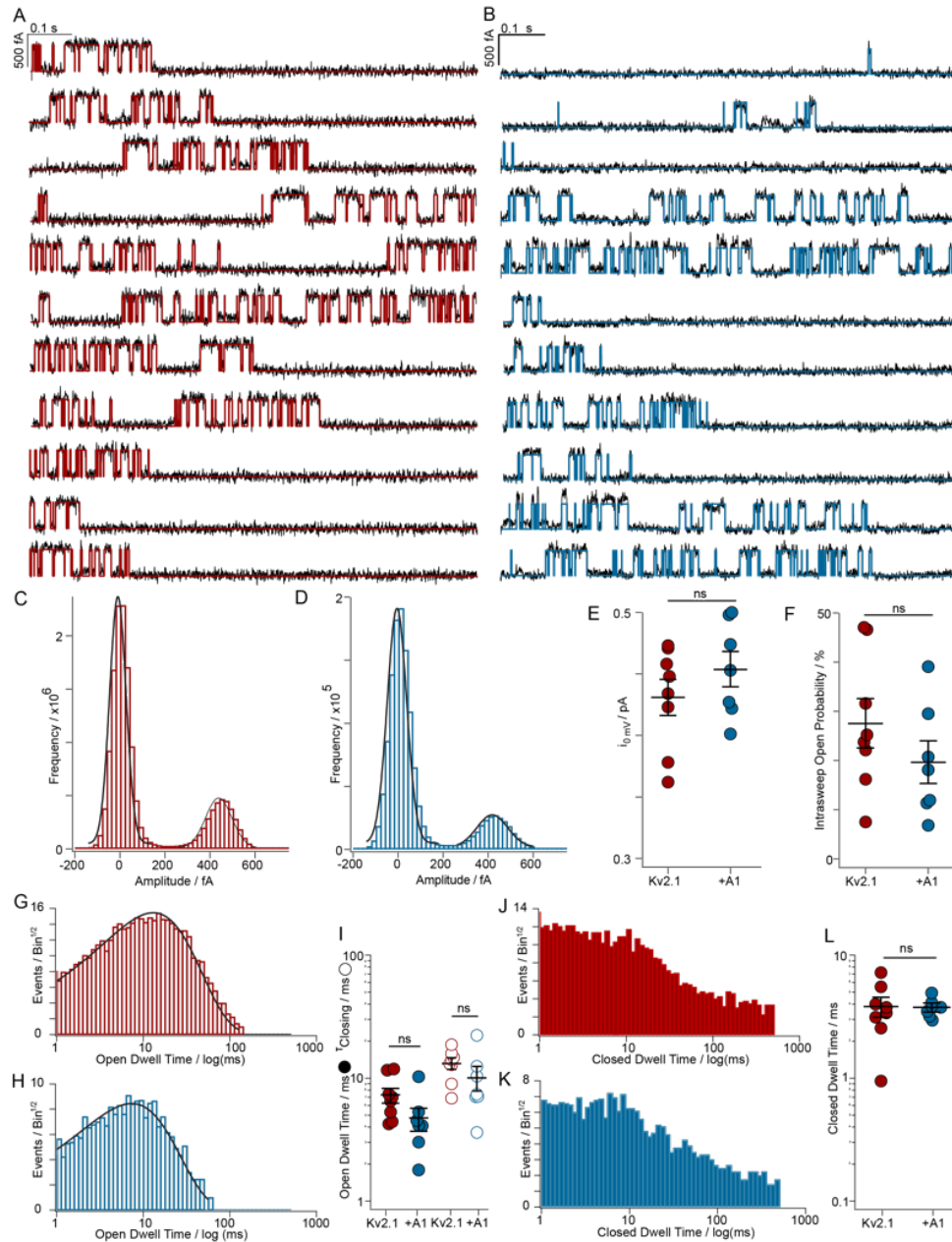


*Figure 4. Effects of AMIGO1 on pore opening conformational changes were not apparent in single channel recordings.*

(A) Representative single channel currents at 0 mV from Kv2.1–control and (B) Kv2.1 + AMIGO1. Red or blue lines are idealizations. (C,D) Amplitude histograms at 0 mV from the patches in A,B fit with Gaussians. (E) Mean single channel current amplitude: Kv2.1–control  $0.43 \pm 0.01$  pA, Kv2.1 + AMIGO1  $0.45 \pm 0.02$  pA. (F) Open probability from amplitude histograms: Kv2.1–control  $28 \pm 4.9\%$ , Kv2.1 + AMIGO1  $20 \pm 4.2\%$ . (G) Open dwell-time distributions and single exponential fits for a Kv2.1–control or (H) Kv2.1 + AMIGO1 patch. (I) Open dwell times from mean (filled circles) or exponential fit (hollow circles). Kv2.1–control:  $13.0 \pm 1.3$   $\mu$ s. Kv2.1 + AMIGO1:  $9.98 \pm 2.3$   $\mu$ s. (J) Closed dwell-time distributions and single exponential fit for a Kv2.1–control or (K) Kv2.1 + AMIGO1 patch. (L) Closed dwell times from mean. Kv2.1–control:  $3.80 \pm 0.67$   $\mu$ s. Kv2.1 + AMIGO1:  $3.73 \pm 0.250$   $\mu$ s. ns = two-tailed t-test p-value > 0.05. Means  $\pm$  SEM.

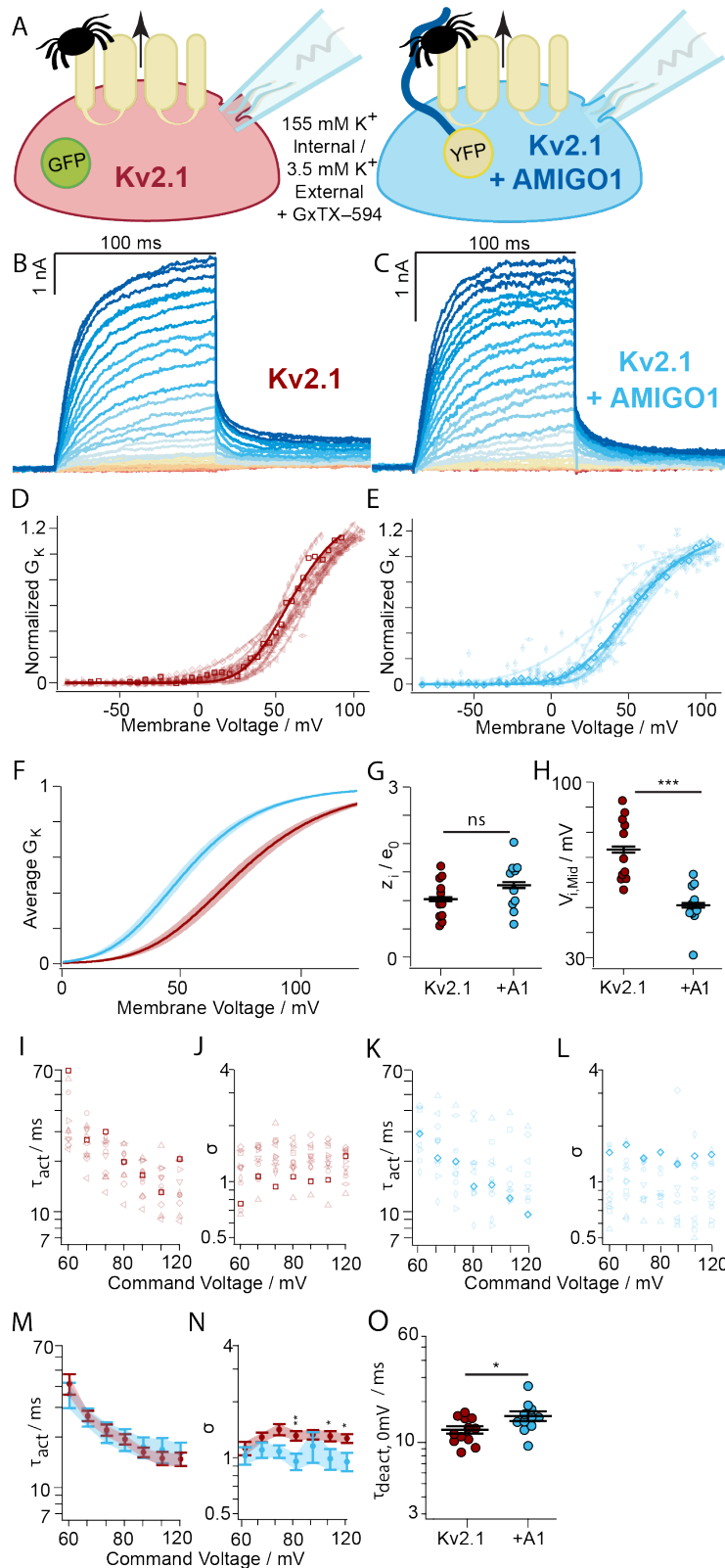
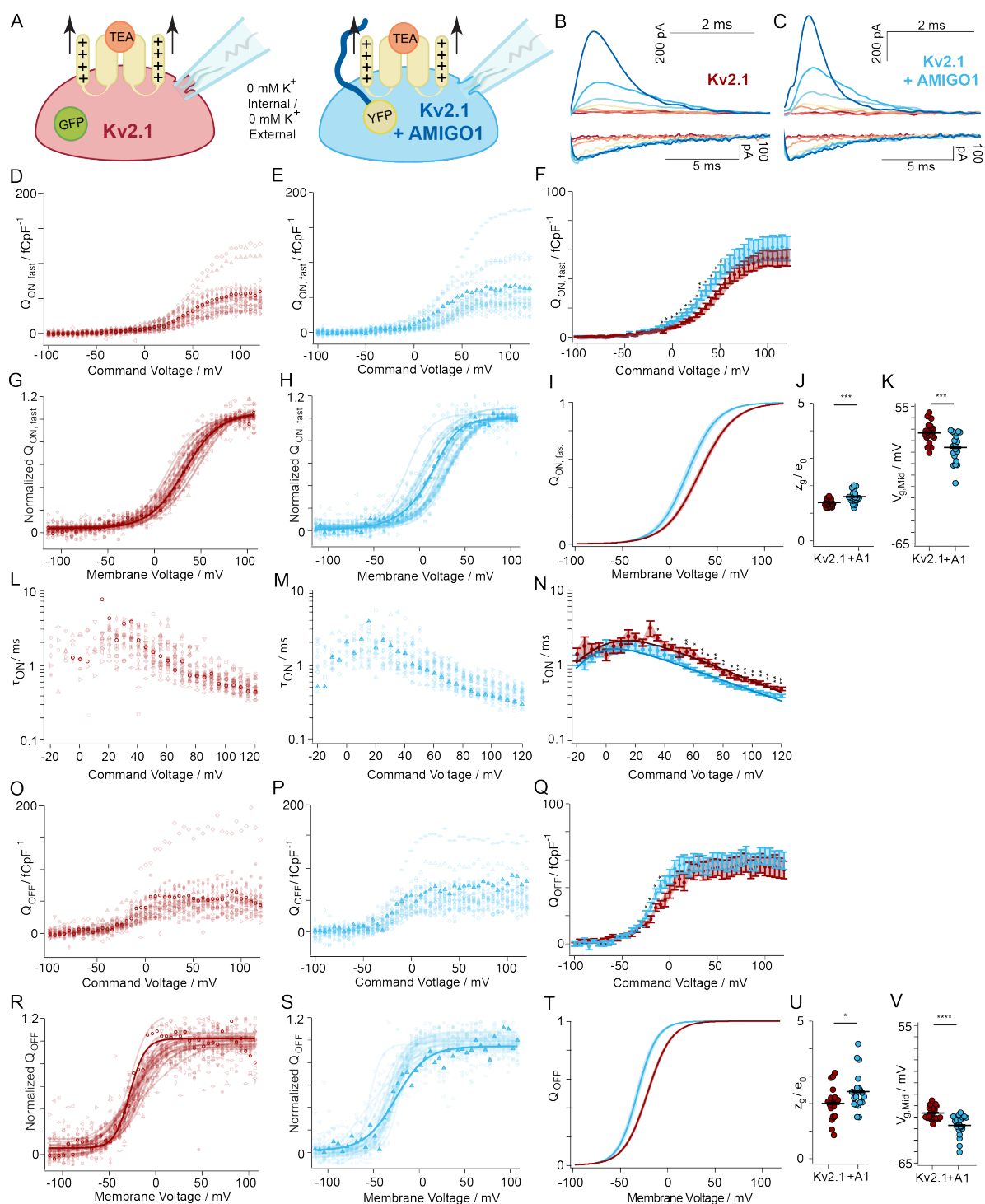


Figure 5. The voltage sensor toxin GxTX-594 enhances AMIGO1 modulation of Kv2.1 conductance. (A) Experimental set up: Whole-cell  $K^+$  currents (arrow) from Kv2.1-CHO transfected with GFP (red) or AMIGO1-YFP (blue). Cells were treated with 100 nM GxTX-594 (tarantulas). (B, C) Representative Kv2.1-control (6.0 pF) or Kv2.1 + AMIGO1 (14.5 pF) cell. Same voltage protocol and representations as Fig. 3. (D, E) Normalized  $G-V$  relationships (F) Reconstructed 4<sup>th</sup> order Boltzmann fits from  $V_{i,Mid}$  and  $z_i$  in Table 1. Shading  $V_{i,Mid} \pm SEM$ . (G) Steepness and (H) midpoint of fits. (I, K)  $\tau_{act}$  and (J, L)  $\sigma$  from fits of Eqn. F to activation (M) Mean  $\tau_{act}$  and (N)  $\sigma$ . (O)  $\tau_{deact}$  fits of Eqn. G to 0 mV tails: Kv2.1 with GxTX-594 =  $12.4 \pm 2.7$  ms. Kv2.1+AMIGO1 with GxTX-594 =  $15.7 \pm 4.2$  ms. All other statistics in Table 1. **\*\*\***:  $p \leq 0.001$ , **\*\***:  $p \leq 0.01$ , **\***:  $p \leq 0.05$ , ns: not significant. Bars are mean  $\pm$  SEM.



**Figure 6. AMIGO1 facilitates the activation of Kv2 voltage sensors.**

(A) Experimental set up: Gating currents (arrows) from Kv2.1–CHO transfected with GFP (red) or AMIGO1–YFP (blue). K<sup>+</sup> currents were eliminated removal of K<sup>+</sup> ions and the external tetraethylammonium, a Kv2 pore-blocker (orange). (B, C) Top/Bottom: Representative I<sub>g,ON</sub>/I<sub>g,OFF</sub> from Kv2.1–control (11.9 pF) or Kv2.1 + AMIGO1 (8.2 pF). Cells were given 100 ms voltage steps ranging from -100 mV (dark red trace) to +120 mV to record I<sub>g,ON</sub> and then stepped to -140 mV to record I<sub>g,OFF</sub>. The holding potential was -100 mV. Voltage pulses to -100, -50, -25, +0, +25, +50, and +100 mV are presented. Data points from representative cells are bolded in analysis panels.

(D, E)  $Q_{ON,fast}/pF-V$  relation from individual cells.  $Q_{ON,fast}/pF$  is gating charge integrated over the first 3.5 ms normalized to cell capacitance. (F) Mean  $Q_{ON,fast}/pF$  (G, H)  $Q_{ON,fast}-V$  relations normalized to maximum  $Q_{ON,fast}$  from +50 to +100 mV voltage steps. Solid lines represent Boltzmann fit (Eqn. C). (I) Reconstructed Boltzmann fits from average  $V_{g,Mid,ON,fast}$  and  $z_{g,ON,fast}$  (Table 2). Shading  $V_{g,Mid,ON,fast} \pm SEM$ . (J) Steepness and (K) midpoint of Boltzmann fits. (L, M)  $\tau_{ON}$  from individual cells fit with Eqn. I. (N) Average  $\tau_{ON}-V$ . Solid lines are Eqn. I fit. Fit values  $\pm SD$  for Kv2.1-control cells:  $\alpha_{0mV} = 254 \pm 26 s^{-1}$ ,  $z_{\alpha} = 0.468 \pm 0.026 e_0$ ,  $\beta_{0mV} = 261 \pm 50 s^{-1}$ ,  $z_{\beta} = -1.31 \pm 0.37 e_0$ ; for Kv2.1 + AMIGO1 cells:  $\alpha_{0mV} = 443 \pm 26 ms^{-1}$ ,  $z_{\alpha} = 0.405 \pm 0.019 e_0$ ,  $\beta_{0mV} = 157 \pm 52 ms^{-1}$ ,  $z_{\beta} = -2.00 \pm 0.55 e_0$ . (O, P)  $Q_{OFF}/pF$  relation from individual cells normalized to cell capacitance. (Q)  $Q_{OFF}/pF-V$  relation. (R, S)  $Q_{OFF}-V$  relations normalized to maximum  $Q_{OFF}$  from +50 to +100 mV voltage steps. Solid lines are Boltzmann fits (Eqn. C). (T) Reconstructed Boltzmann fits using the average  $V_{g,Mid,OFF}$  and  $z_{g,OFF}$  (Table 2). Shading  $V_{g,Mid,OFF} \pm SEM$  (U) Steepness and (V) midpoint of Boltzmann fits. Mean  $\pm SEM$ . Statistics in Table 2. \*\*\*\*:  $p \leq 0.0001$ , \*\*\*:  $p \leq 0.001$ , \*\*:  $p \leq 0.01$ , \*:  $p \leq 0.05$ , ns: not significant. Bars are mean  $\pm SEM$ .

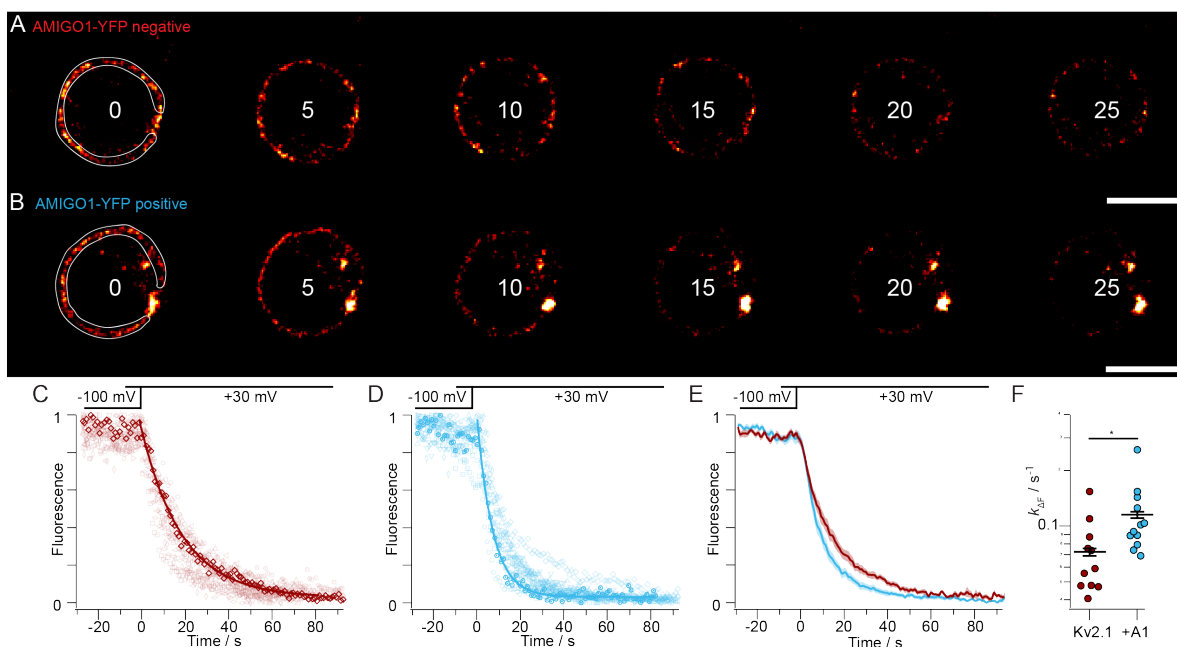


*Figure 7. AMIGO1 accelerates voltage-stimulated GxTX-594 dissociation.*

(A, B) Fluorescence from the solution-exposed membrane of voltage-clamped Kv2.1-CHO cells  $\pm$  AMIGO1-YFP. Kv2.1 expression was achieved through a 48-hour induction period. Cells were held at -100 mV for 30 seconds before being stimulated to +30 mV (time = 0 s) to trigger GxTX-594 dissociation. The time point in seconds of each image is listed. Region of interest for analysis is shown by the white line in left panel, which excludes the point contact with pipette and intracellular regions which have voltage-insensitive fluorescence. 10  $\mu$ m scale bar. (C, D) Normalized fluorescence intensity decay plots for Kv2.1-CHO cells without (red) and with (blue) AMIGO1-YFP fluorescence. The bolded traces correspond to exemplar cells in (A) and (B). Solid line is monoexponential fit (Eqn. G). (E) Averaged fluorescence intensity decay for AMIGO1-YFP negative (red), and AMIGO1-YFP positive (blue) cells. SEM is shaded. (F) Rates of fluorescence change ( $k_{AF}$ ) were calculated as  $1/\tau$  from Eqn. G fits. \*:  $p = 0.03$  unpaired, two-tailed, t-test

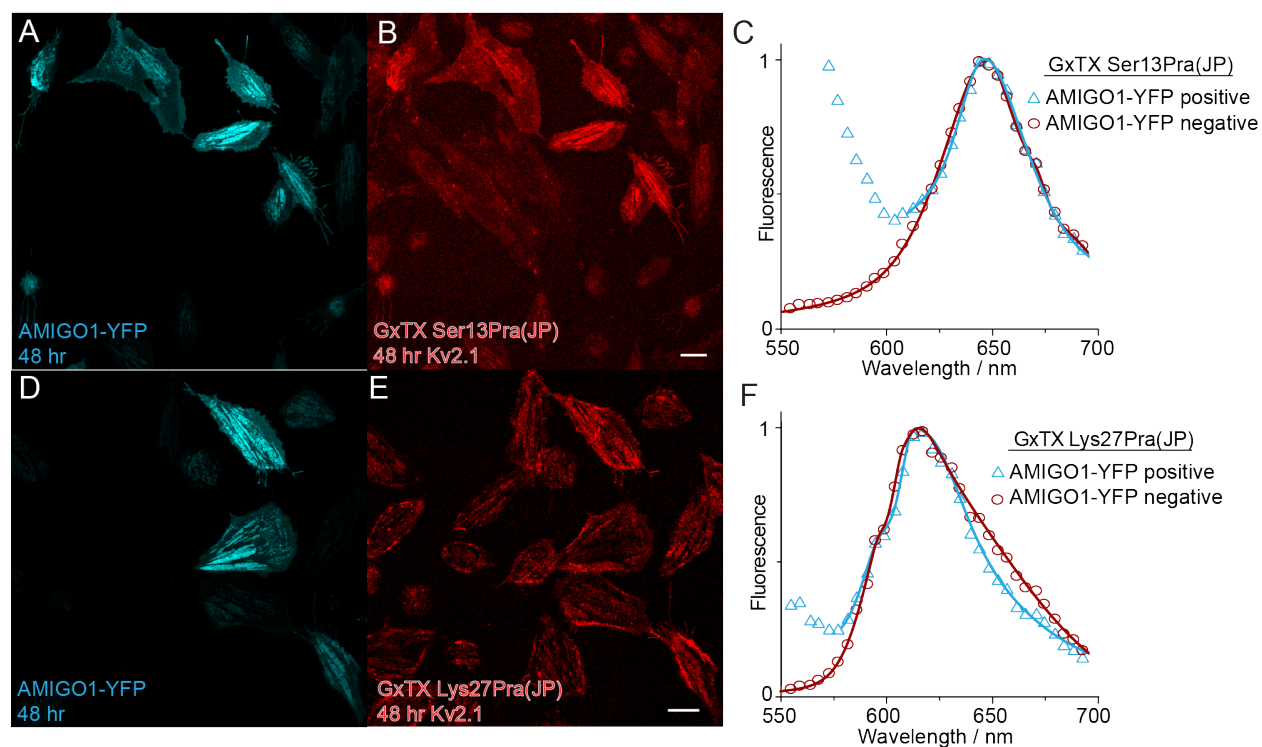


*Figure 8. AMIGO1 does not alter the Kv2.1–GxTX interface on resting voltage sensors.*

Kv2.1–CHO cells transfected with AMIGO1–YFP were treated with GxTX Ser13Pra(JP) or GxTX Lys27Pra(JP) (**A**, **D**) Confocal image of AMIGO1–YFP fluorescence (blue) and (**B**, **E**) JP fluorescence. (**C**, **F**) Fitted emission spectra of cells positive (blue) and negative (red) for AMIGO1–YFP fluorescence. Data points for all spectra are the mean of normalized emission from AMIGO1–YFP positive cells and AMIGO1–negative cells. Spectra were fit with two–component split pseudo–Voigt functions with shape parameters and root–mean–squared values found in Supplemental Table 1.

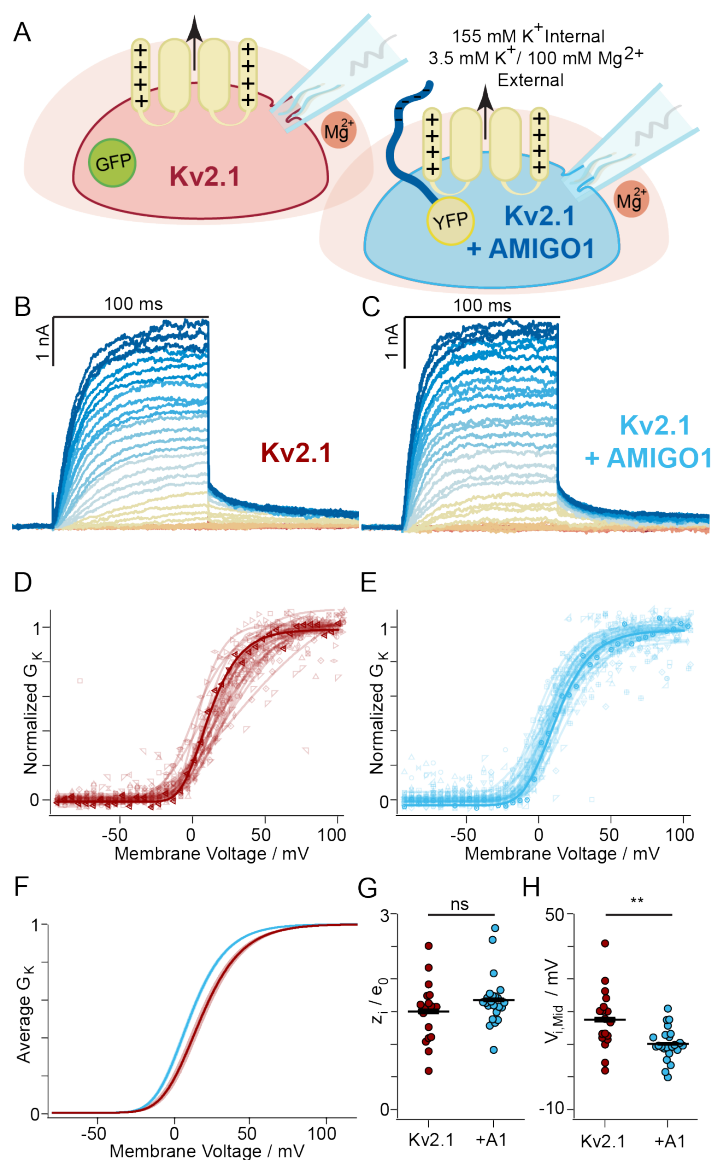


**Figure 9. Surface charge screening does not suppress the AMIGO1 effect.**

(A) Experimental set up: Whole-cell K<sup>+</sup> currents (arrow) from Kv2.1–CHO transfected with GFP (red) or AMIGO1–YFP (blue). 100 mM magnesium was used to shield surface charges (peach halo). Same voltage protocol and representations as Fig. 3. (B, C) Representative Kv2.1–control (10.0 pF) or Kv2.1 + AMIGO1 (6.3 pF) cell. (D, E) Normalized  $G-V$  relationships. (F) Reconstructed 4<sup>th</sup> order Boltzmann fits from average  $V_{i, Mid}$  and  $z_i$  (Table 1). Shading  $V_{i, Mid} \pm$  SEM. (G) Steepness and (H) midpoint of 4<sup>th</sup> order Boltzmann fits. Mean  $\pm$  SEM. Statistics in Table 1. \*\*:  $p = \leq 0.01$ , ns: not significant.

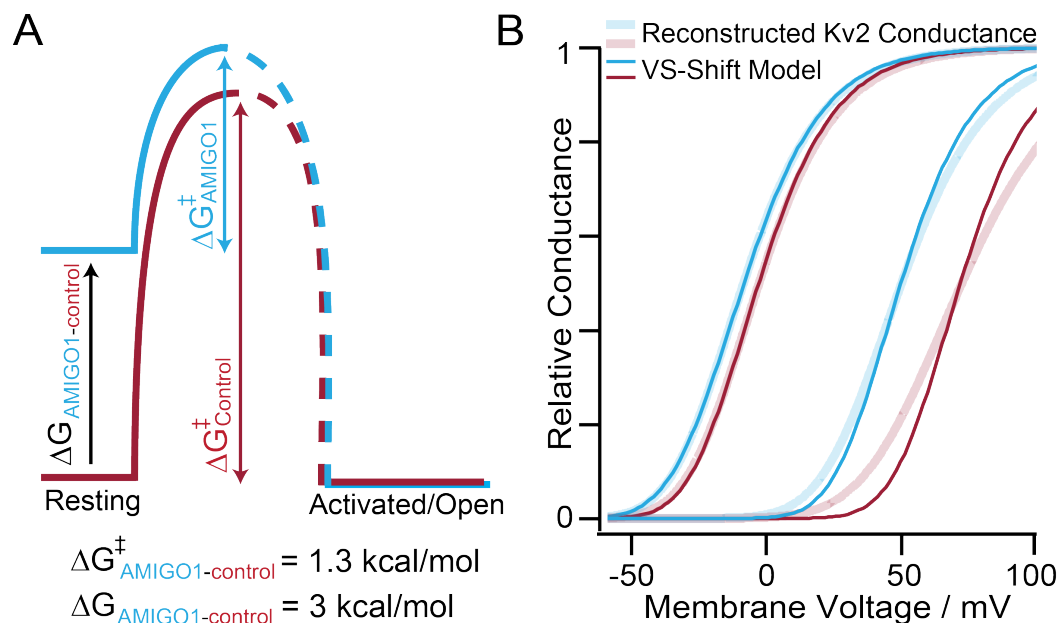


Figure 10. AMIGO1 destabilizes the resting conformation of Kv2.1 voltage sensors.

(A) AMIGO1 raises resting state energy ( $\Delta G$ ) of Kv2.1 voltage sensors and lowers the energy barrier ( $\Delta G^{\ddagger}$ ) of Kv2.1 activation. (B) Voltage sensor shift model of AMIGO1 modulation (dark lines) plotted with reconstructed  $G$ - $V$ s from Kv2.1-CHO Table 1 values (pale lines). From left to right: Kv2.1+AMIGO1, Kv2.1-Control, Kv2.1+AMIGO1 with GxTX-594, Kv2.1-Control with GxTX-594. Voltage sensor shift model is  $f(V) = \left(1 + e^{-(V-V_{\text{VSD},1/2})^2/25.46}\right)^{-4} \cdot \left(1 + e^{-(V-V_{\text{Pore},1/2})^2/25.46}\right)^{-1}$ , where  $z = 1.5 e_0$ ,  $V_{\text{Pore},1/2} = -16 \text{ mV}$ , and  $V_{\text{VSD},1/2}$  varies. Kv2.1-Control  $V_{\text{VSD},1/2} = -33 \text{ mV}$  and Kv2.1-Control with GxTX-594  $V_{\text{VSD},1/2} = 51 \text{ mV}$ . AMIGO1  $\Delta V_{\text{VSD},1/2} = -22 \text{ mV}$  with or without GxTX-594.

	<i>G-V</i> fit parameters				$\Delta G_{AMIGO1}$ (kcal/mol)
	$V_{i,1/2}$ (mV)	$V_{i,Mid}$ (mV)	$z_i$ ( $e_0$ )	$n$	(Eqn. E)
<b>HEK293 cells</b>					
mKv2.1 + GFP	-26.8 ± 3.0	-1.7 ± 1.4 <sup>A</sup>	1.79 ± 0.17 <sup>D</sup>	7	-0.31
mKv2.1 + AMIGO1 + GFP	-30.9 ± 0.8	-7.4 ± 1.8 <sup>B</sup>	1.95 ± 0.16 <sup>E</sup>	14	
mKv2.1 + SCNβ1 + GFP	-24.8 ± 1.5	0.2 ± 1.8 <sup>C</sup>	1.720 ± 0.074 <sup>F</sup>	8	
<b>Kv2.1-CHO cells</b>					
rKv2.1 + GFP	-33.4 ± 1.7	-1.8 ± 1.2 <sup>G</sup>	1.411 ± 0.070 <sup>I</sup>	20	-0.28
rKv2.1 + AMIGO1-YFP	-42.0 ± 3.3	-7.6 ± 1.8 <sup>H</sup>	1.40 ± 0.11 <sup>J</sup>	19	
<b>Kv2.1-CHO cells + Mg<sup>2+</sup></b>					
rKv2.1 + GFP	-13.8 ± 1.8	17.6 ± 2.2 <sup>K</sup>	1.51 ± 0.11 <sup>M</sup>	18	-0.37
rKv2.1 + AMIGO1-YFP	-16.3 ± 1.5	10.2 ± 1.0 <sup>L</sup>	1.682 ± 0.082 <sup>N</sup>	23	
<b>Kv2.1-CHO cells + GxTX-594</b>					
rKv2.1 + GFP	26.8 ± 2.9	73.2 ± 3.8 <sup>O</sup>	1.03 ± 0.11 <sup>Q</sup>	13	-0.77
rKv2.1 + AMIGO1-YFP	12.9 ± 4.4	50.9 ± 2.8 <sup>P</sup>	1.27 ± 0.14 <sup>R</sup>	12	

**Table 1. Fourth order Boltzmann parameters for *G-V* relationships.**

Average  $V_{i,1/2}$ ,  $V_{i,Mid}$ , and  $z_i$  values were derived from a 4<sup>th</sup> order Boltzmann fits (Eqn. C) of  $n$  individual cells. All values are given ± SEM. Brown-Forsythe and Welch (appropriate for differing SD) ANOVA test with a Dunnett's T3 multiple comparisons p-values: AB: 0.046. AC: 0.64. DE: 0.75. DF: 0.91. Unpaired, two-tailed t-test p-values: GH: 0.012. IJ: 0.95. KL: 0.0051. MN: 0.21. OP: 0.00018. QR: 0.19.  $\Delta G_{AMIGO1}$  from Eqn. E, at  $V_{i,Mid}$  for Kv2.1 + GFP.

<b>Kv2.1-CHO cells</b>	<i>Q-V</i> fit parameters				$\Delta G_{AMIGO1}$ (kcal/mol)		
	$Q_{ON,fast}$	$V_{g,Mid}$ (mV)	$z_g$ ( $e_0$ )	$n$	Eqn. E		
rKv2.1 + GFP		30.6 ± 2.0 <sup>S</sup>	1.38 ± 0.03 <sup>U</sup>	20	-1.92		
rKv2.1 + AMIGO1-YFP		17.8 ± 2.9 <sup>T</sup>	1.61 ± 0.05 <sup>V</sup>	20			
$Q_{OFF}$	$V_{g,Mid}$ (mV)	$V_{g,Med}$ (mV)	$z_g$ ( $e_0$ )	$n$	Eqn. E	Eqn. K*	Eqn. K*°
rKv2.1 + GFP	-22.0 ± 1.3 <sup>W</sup>	-19.5	2.00 ± 0.13 <sup>Y</sup>	20	-2.45	-3.11 ± 0.69	-2.74
rKv2.1 + AMIGO1-YFP	-32.8 ± 2.0 <sup>X</sup>	-29.0	2.43 ± 0.15 <sup>Z</sup>	20			

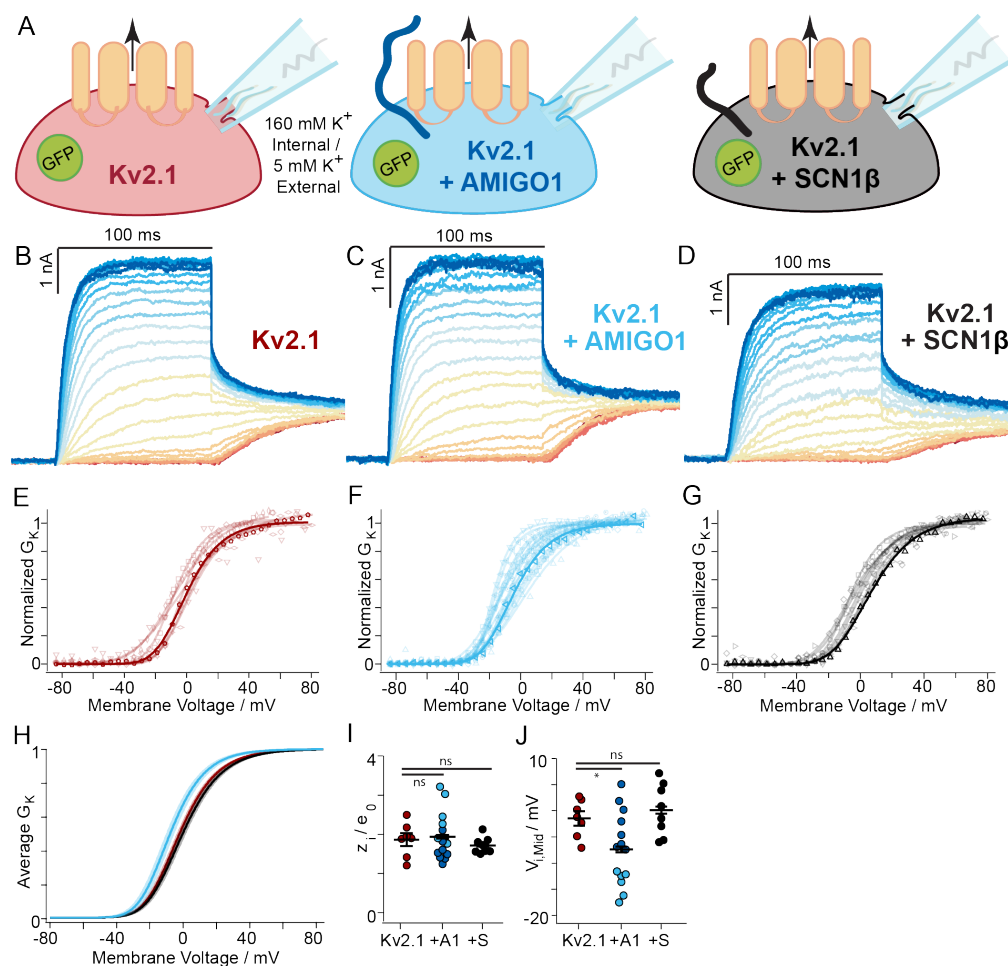
**Table 2. Boltzmann parameters and  $\Delta G$  calculations for voltage sensor movement.**

Average  $V_{g,Mid}$  and  $z_g$  values were derived from 1<sup>st</sup> order Boltzmann fits of  $n$  individual cells. Means ± SEM.  $V_{g,Mid} = V_{g,1/2}$ .  $V_{g,Med}$  is median voltage (58). Unpaired, two-tailed t-test p-values:  $Q_{ON,fast}$ : ST: 0.00093. UV: 0.00084. OFF Gating currents: WX:  $7.82 \times 10^{-5}$ . YZ: 0.038. \* $z = 12.5 e_0$ , °  $V_{g,Med}$  was used.

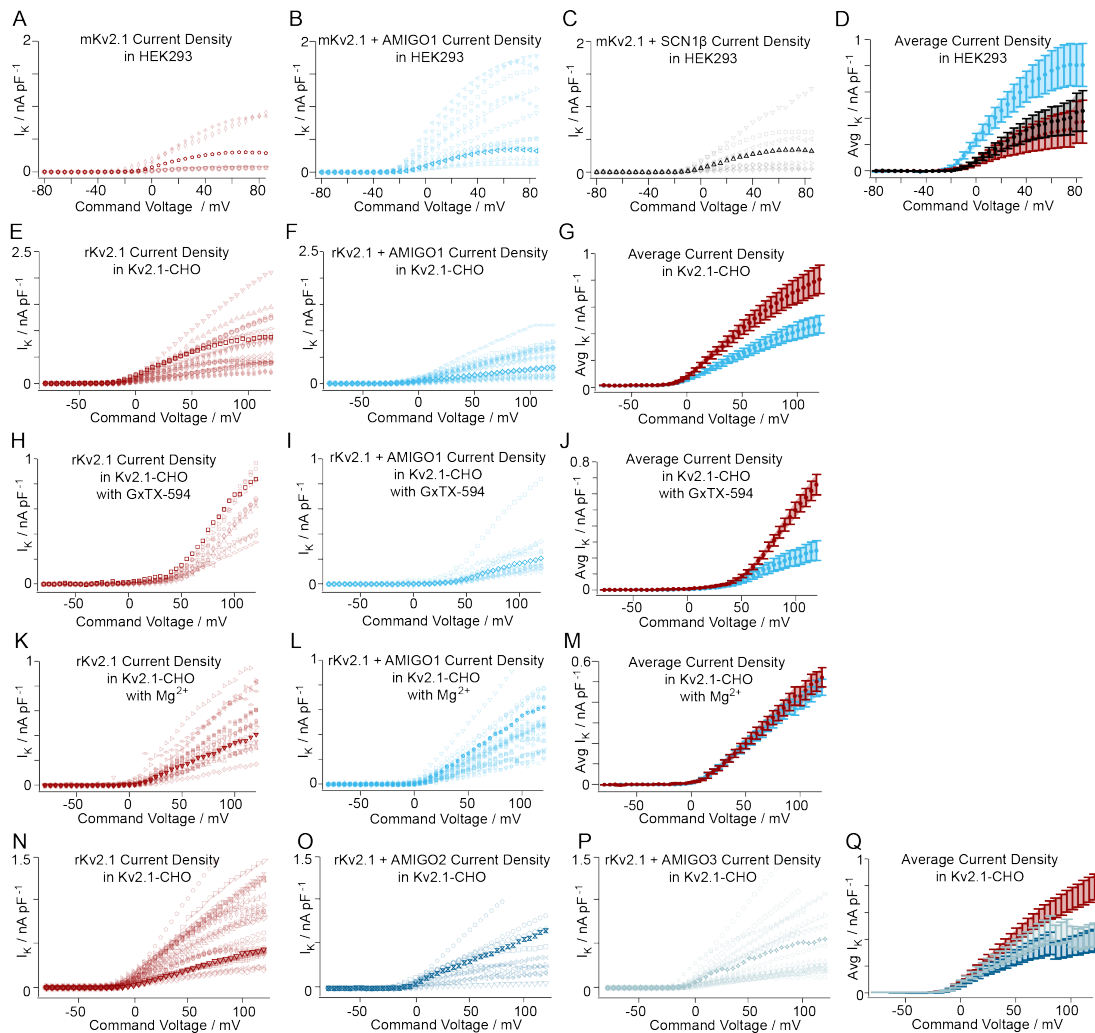
Calculated activation of native Kv2 conductance after 1.5 ms at 0 mV			
Type of AMIGO1 impact	$\tau_{0mV}$ (s)	$V_{Mid}$ (mV)	Relative Conductance
none, values from (7)	0.0029	-13.1	0.022
from conductance data	0.0040 <sup>†</sup>	-7.1	0.0067
from voltage sensor data	0.0050 <sup>†</sup>	-2.3	0.0024

**Table 3. Prediction of AMIGO1 impacts on Kv2 conductance in superior cervical ganglion neurons.**

Liu and Bean fit Kv2 kinetics with  $(1 - e^{-t/\tau_{0mV}})^4$  and the *G-V* with  $(1 + e^{-(V-V_{Mid})/k})^{-1}$ , and these equations are used to calculate relative conductance here  $\tau_{0mV}$  and  $\Delta V_{Mid}$  adjusted for the impact of loss of AMIGO1 from Kv2.1-CHO cells. The AMIGO1 impact on conductance activation was a 1.38-fold acceleration of  $\tau_{0mV}$  (Fig. 3M) and *G-V*  $\Delta V_{i,Mid} = -5.7$  mV (Table 1). The AMIGO1 impact on voltage sensor activation was a 1.74-fold acceleration of  $\tau_{0mV}$  (change in  $\alpha_{0mV}$  from fit in Fig. 6N) and  $Q_{OFF-V} \Delta V_{g,Mid} = -10.8$  mV (Table 2).

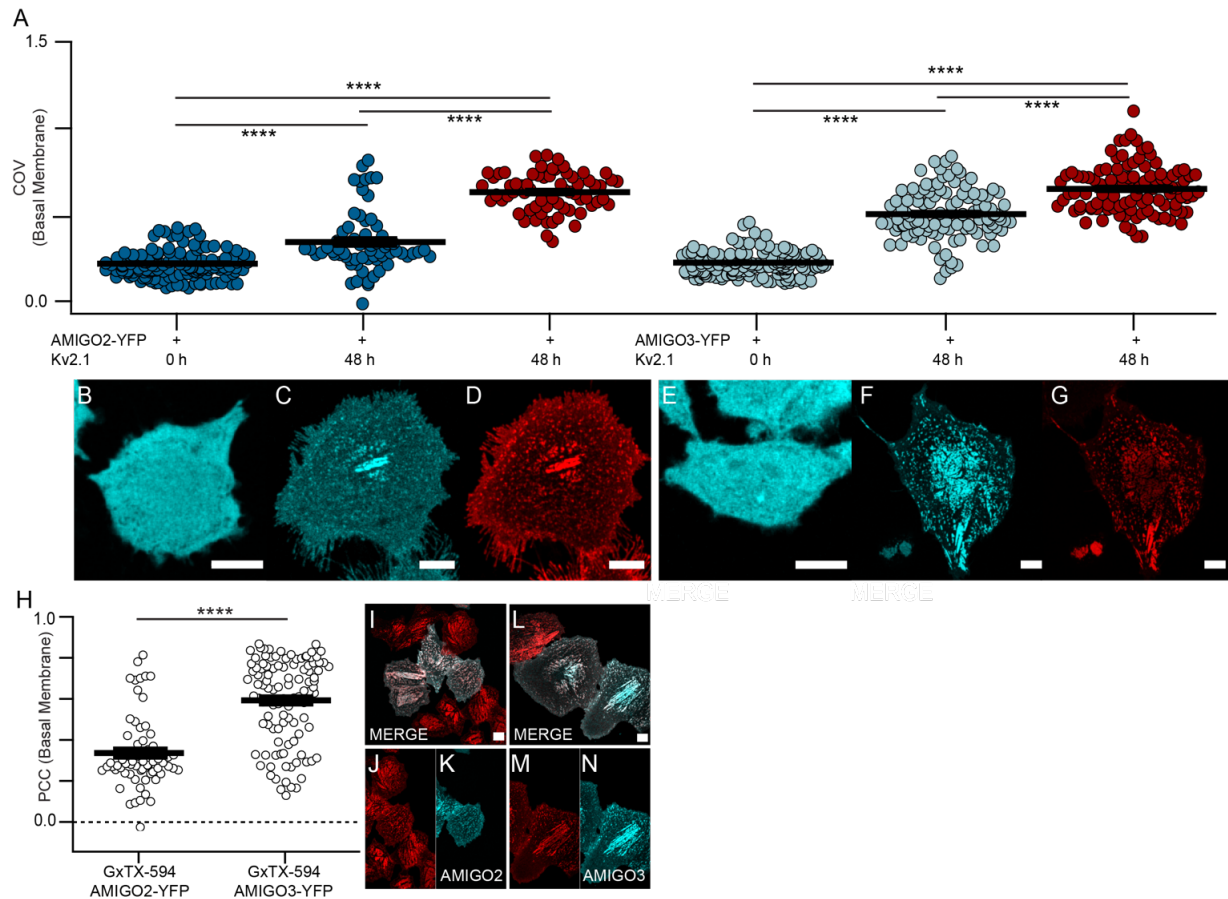


**Supplemental Figure 1. AMIGO1, but not SCN1β, modulates Kv2.1 conductance in HEK293 cells.** (A) Experimental set up: Whole-cell K<sup>+</sup> currents from HEK293 cells co-transfected with mKv2.1 and either GFP (red), or AMIGO1-pIRES2-GFP (blue), or SCN1β-pIRES2-GFP (black). (B, C, D) Representative mKv2.1-control (14.8 pF), mKv2.1 + AMIGO1 (9.6 pF), or mKv2.1 + SCN1β (10.0 pF) HEK293 cell. Data points from representative cells are bolded in analysis panels. (E, F, G) Normalized  $G-V$  relationships for mKv2.1-control, mKv2.1 + AMIGO1, or mKv2.1 + SCN1β cells. Symbols correspond to individual cells. Lines are 4<sup>th</sup> order Boltzmann relationships (Eqn. C). (H) Reconstructed 4<sup>th</sup> order Boltzmann fits using the average  $V_{i,Mid}$  and  $z_i$  (Table 1). Shaded areas represent  $V_{i,Mid} \pm SEM$ . (I) Steepness and (J) midpoint of 4<sup>th</sup> order Boltzmann fits. For the mKv2.1 + AMIGO1 cells, individual  $V_{i,Mid}$  and  $z_i$  values are displayed in dark or light blue to highlight an increase in variability. Specifically, the standard deviation of  $V_{i,Mid}$  increased from  $\pm 3.6$  mV in control cells to  $\pm 6.9$  mV in mKv2.1 + AMIGO1 cells. We note that the  $V_{i,Mid}$  values for mKv2.1 + AMIGO1 cells seemed to partition into two groups: a more negatively shifted group with an average  $V_{i,Mid}$  of -13.9 mV (light blue), and a group similar to mKv2.1 alone with an average  $V_{i,Mid}$  of -2.5 mV (dark blue). Although all cells analyzed had GFP fluorescence indicating transfection with the AMIGO1-pIRES2-GFP vector, it is possible that some cells were not expressing sufficient AMIGO1 to have a functional effect. Statistics in Table 1. \*:  $p \leq 0.05$ , ns: not significant. Bars are mean  $\pm$  SEM.



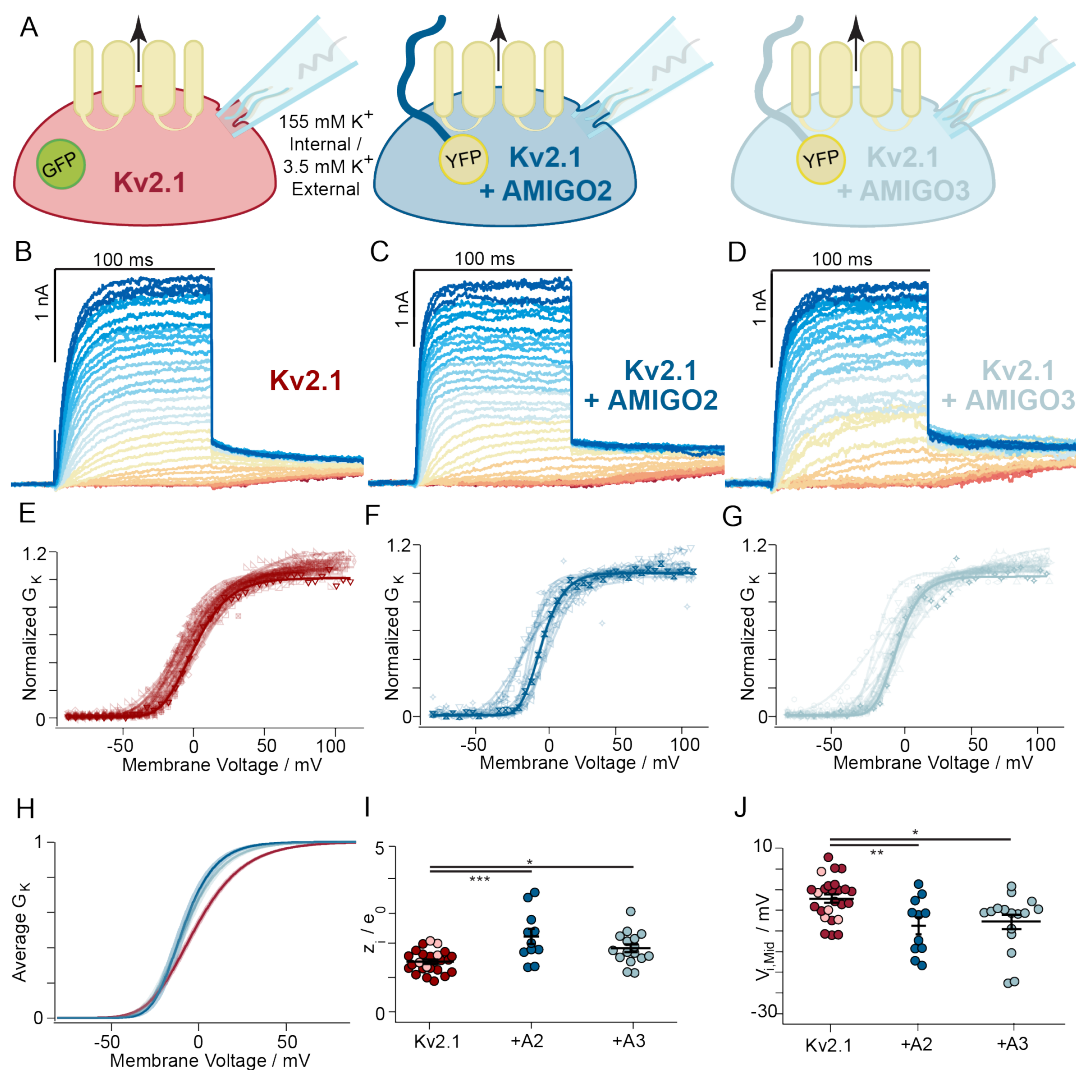
*Supplemental Figure 2. Kv2.1 current density ± AMIGO1 in HEK293 and Kv2.1-CHO cells.*

AMIGO1 has mixed effects on current density in HEK293 and Kv2.1-CHO cells. Outward current densities normalized by cell capacitance were calculated from mean of the last 10 ms of each voltage step and plotted against the command voltage. Symbols represent individual cells. (A, B, C) HEK293 cells co-transfected with mKv2.1 + GFP, mKv2.1 + AMIGO1-pIRES2-GFP, or mKv2.1 + SCN1β-pIRES2-GFP. To limit the proportion of currents from endogenous voltage-dependent channels (53, 60), we set a minimum outward current density as an inclusion threshold for analysis (65 pA/pF at +85 mV). Of the cells patched, 7 of 18 mKv2.1-control cells, 14 of 28 mKv2.1 + AMIGO1 cells, and 8 of 27 mKv2.1 + SCN1β cells satisfied this inclusion threshold and displayed currents consistent with a Kv2.1 delayed rectifier conductance ( $I_k$ ). Cells that did not meet the inclusion criteria are not plotted making the full variability of current densities is extreme than depicted here. Bolded symbols are exemplars from Supplemental Fig. 1B, C, or D. (D) Averages of A, B, and C. (E, F) Kv2.1-CHO ± AMIGO1-YFP. Bolded symbols are exemplars from Fig. 3B or 3C. (G) Averages of E and F. (H, I) Kv2.1-CHO ± AMIGO1-YFP in 100 nM GxTX-594. Bolded symbols are exemplars from Fig. 5B or 5C. Cell symbols matched between E/H and F/I before and after GxTX-594 addition. (J) Averages of H and I. (K, L) Kv2.1-CHO ± AMIGO1-YFP in 3.5 mM  $K^+$ /100 mM  $Mg^{2+}$  external. Bolded symbols are exemplars from Fig. 9B or 9C. (M) Averages of E and F. Averaged data are means ± SEM.



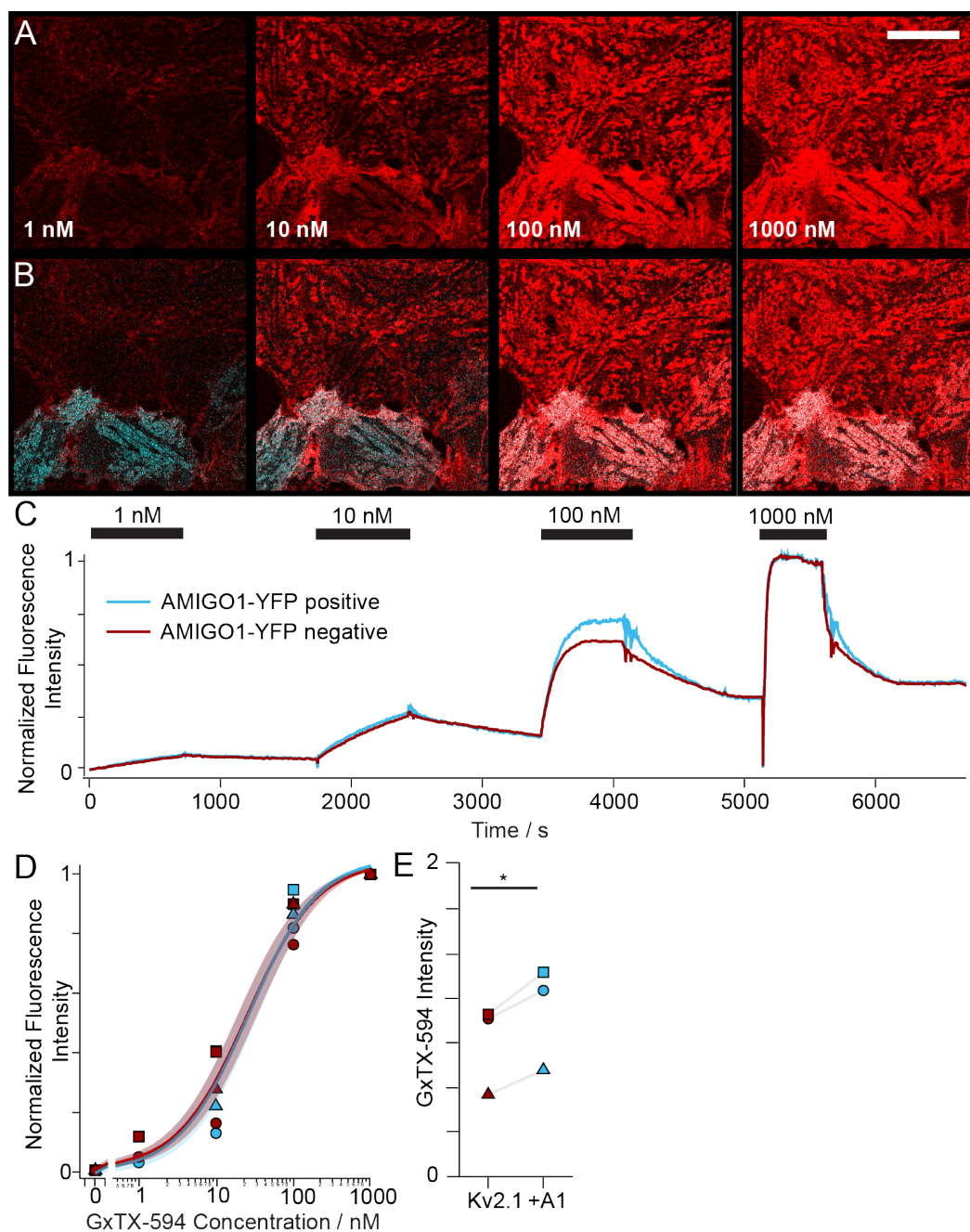
*Supplemental Figure 3. Kv2.1 reorganizes and colocalizes with AMIGO homologs in CHO cells.*

**(A)** Coefficient of variation of fluorescence from AMIGO2–YFP (dark blue circles), AMIGO3–YFP (light blue circles), or GxTX–594 (red circles). COV from confocal images of glass–adhered membranes (exemplar images in **B–G**). AMIGO2–YFP fluorescence from cells **(B)** not induced for Kv2.1 expression ( $COV_{A2,0h} = 0.2090 \pm 0.0062$ ,  $n = 144$ ), **(C)** induced 48 h for Kv2.1 expression ( $COV_{A2,48h} = 0.342 \pm 0.022$ ,  $n = 65$ ). **(D)** GxTX–594 labeling of the cells in **C** ( $COV_{A2,48h(GxTX-594)} = 0.631 \pm 0.013$ ,  $n = 65$  cells). AMIGO3–YFP fluorescence from cells **(E)** not induced for Kv2.1 expression ( $COV_{A3,0h} = 0.2186 \pm 0.0052$ ,  $n = 160$ ), **(F)** induced 48 h for Kv2.1 expression ( $COV_{A3,48h} = 0.503 \pm 0.014$ ,  $n = 109$ ). **(G)** GxTX–594 labeling of the cells in panel **F** ( $COV_{A3,48h(GxTX-594)} = 0.650 \pm 0.013$ ,  $n = 109$  cells). **(H)** Costes thresholded, Pearson’s colocalization coefficients from cells induced for Kv2.1 expression 48 h prior to imaging. From left to right:  $PCC_{A2,GxTX-594} = 0.342 \pm 0.022$ ,  $\geq 0$  ( $p < 0.0001$ , one–tailed, t–test),  $n = 65$ ;  $PCC_{A3,GxTX-594} = 0.597 \pm 0.020$ ,  $\geq 0$  ( $p < 0.0001$ , one–tailed, t–test),  $n = 108$ . **(I, J, K)** Exemplar images where merge overlay (white) shows colocalization between GxTX–594 (red) and AMIGO2–YFP (cyan) or **(L, M, N)** AMIGO2–YFP (cyan) Arithmetic means and standard errors are plotted. **(Statistics)** Outliers were removed using ROUT,  $Q = 1\%$ . An ordinary one–way ANOVA with multiple comparisons was used to evaluate the differences between groups in COV analysis, while a t–test was used to evaluate the PCC data. \*\*\*\*:  $p = \leq 0.0001$ . Bars are mean  $\pm$  SEM. All scale bars are 10  $\mu$ m.



Supplemental Figure 4. AMIGO2 and AMIGO3 modulate Kv2.1 conductance in CHO cells.

**(A)** Experimental set up: Whole-cell  $K^+$  currents (arrow) from Kv2.1–CHO transfected with GFP (red), rAMIGO2–YFP (dark blue), or rAMIGO3–YFP (light blue). Same voltage protocols and representation as Fig. 3. **(B, C, D)** Representative Kv2.1–control (5.1 pF), Kv2.1 + AMIGO2 (6.6 pF) or Kv2.1 + AMIGO3 (2.4 pF) cells. **(E, F, G)** Normalized  $G$ - $V$  relationships. 5 of the Kv2.1–control cells were recorded from side by side with the Kv2.1 + AMIGO3 cells and Kv2.1 + AMIGO2 cells and Kv2.1 + AMIGO1 recordings for Fig. 3 (assessed by t-test), and data was pooled. Solid lines a 4<sup>th</sup> order Boltzmann fits (Eqn. C). **(H)** Reconstructed 4<sup>th</sup> order Boltzmann fits from average  $V_{i, Mid}$  and  $z_i$  (Supplemental Table 1). Shading  $V_{i, Mid} \pm SEM$ . **(I)** Steepness and **(J)** midpoint of fits. Statistics in Table 1. \*\*\*:  $p = \leq 0.001$ , \*\*:  $p = \leq 0.01$ , \*:  $p = \leq 0.05$ . Bars are mean  $\pm$  SEM.



*Supplemental Figure 5. AMIGO1 does not impede GxTX-594 binding to Kv2.1.*

(A) Fluorescence from Kv2.1-CHO cells transfected with AMIGO1-YFP, induced for Kv2.1 expression for 48 hours and labeled with indicated concentrations of GxTX-594 (red). Scale bar 20  $\mu\text{m}$ . (B) Overlap (white) between AMIGO1-YFP (cyan) and GxTX-594 fluorescence. (C) Mean fluorescence intensities from ROIs encompassing AMIGO1-YFP positive or negative cells from the concentration-response experiment shown in A. (D) Normalized fluorescence intensity after 500 s at each concentration as in panel C. Symbol shapes represent data from each of 3 experiments. Curves and shaded regions represent the mean  $\pm$  SEM of a Langmuir binding isotherm (Eqn. L) fit to individual experiments.  $K_d = 27.5 \pm 8.3$  nM without and  $27.9 \pm 7.2$  nM with AMIGO1-YFP.  $K_d$  likely is overestimated due to incomplete equilibration at 1 and 10 nM. (E) Cells expressing AMIGO1-YFP had brighter GxTX-594 fluorescence with 1000 nM GxTX-594. Symbols correspond with D.

	<i>G-V</i> fit parameters				$\Delta G_{AMIGOX}$ (kcal/mol)
	$V_{i,1/2}$ (mV)	$V_{i,Mid}$ (mV)	$z_1$ ( $e_0$ )	$n$	(Eqn. E)
<b>Kv2.1-CHO cells</b>					
rKv2.1 + GFP	$-32.5 \pm 1.5$	$-2.0 \pm 1.0^A$	$1.471 \pm 0.067^D$	25	
rKv2.1+ AMIGO2-YFP	$-29.7 \pm 3.4$	$-8.7 \pm 2.1^B$	$2.25 \pm 0.23^E$	11	-0.39
rKv2.1+ AMIGO3-YFP	$-31.8 \pm 2.4$	$-7.8 \pm 1.7^C$	$1.88 \pm 0.12^F$	16	-0.31

*Supplemental Table 1. Fourth order Boltzmann parameters for G-V relationships of AMIGO homologs.*

Average  $V_{i,1/2}$ ,  $V_{i,Mid}$ , and  $z_1$  values were derived from a 4<sup>th</sup> order Boltzmann fits (Eqn. C) of  $n$  individual cells. All values are given  $\pm$  SEM. Ordinary one-way ANOVA test with Dunnett's multiple comparisons p-values: AB: 0.0082. AC: 0.010. DE: 0.0002. DF: 0.026.  $\Delta G_{AMIGO1}$  from Eqn. E, at  $V_{i,Mid}$  for Kv2.1 + GFP.

GxTX(JP) conjugate	AMIGO1-YFP Expression	fitting component	a0	a1	a2	a3	a4	a5	R <sup>2</sup>
<b>GxTX Ser13Pra(JP)</b>	<b>- AMIGO</b>	1	0.229	670.4	47.88	11.41	1.075	2.323	0.999
		2	0.813	647.0	25.73	21.77	0.631	1.685	
	<b>+ AMIGO</b>	1	0.893	646.7	23.30	25.63	1.822	0.721	0.997
		2	0.006	-1610	-15206	-1877	4967	461.2	
<b>GxTX Lys27Pra(JP)</b>	<b>- AMIGO</b>	1	0.352	594.3	12.11	-11.53	0.568	5.364	0.998
		2	0.719	608.2	9.71	59.05	0.359	-0.264	
	<b>+ AMIGO</b>	1	0.715	597.8	16.07	18.08	1.578	2.912	0.997
		2	0.632	616.3	9.05	26.28	-1.657	1.488	

*Supplemental Table 2. Split Pseudo-Voigt fitting parameters.*

Fluorescence emission spectra split pseudo-Voigt fitting parameters and root-mean squared values.

Figure	# Transfections	n per transfection		
Fig. 3	7	peGFP: 5, 2, 2, 4, 1, 2, 4		+AMIGO1: 3, 3, 3, 4, 3, 2, 1
Fig. 4	6	peGFP: 2, 1, 1, 1, 1, 2		+AMIGO1: 1, 2, 1, 3, 0, 0
Fig. 5	5	peGFP: 4, 2, 2, 3, 2		+AMIGO1: 3, 3, 1, 3, 2
Fig. 6	6	peGFP: 5, 4, 4, 2, 1, 4		+AMIGO1: 2, 3, 4, 1, 4, 6
Fig. 7	2	AMIGO1 (-): 6, 5		AMIGO1 (+): 5, 6
Fig. 9	4	peGFP: 1, 3, 4, 10		+AMIGO1: 5, 5, 7, 6
Sup. Fig. 1	4	peGFP: 3, 3, 1, 0	+AMIGO1: 4, 4, 6, 0	+SCNB1: 1, 1, 2, 4
Sup. Fig. 4	5	peGFP: 5, 0, 0, 0, 0 (+peGFP n-values from Fig. 3)	+AMIGO2: 1, 2, 0, 1, 7	+AMIGO3: 1, 7, 5, 0, 3

Supplemental Table 3. N-values for electrophysiology experiments.

Figure	# Transfections	# n values per transfection					
Fig. 1	4	YFP (0 hr): 28, 48, 0, 58	YFP (1.5 hr): 25, 55, 42, 95	YFP (48 hr): 82, 54, 74, 67	YFP (ChR): 11, 21, 32, 61	GxTX-594 (48 hr, AMIGO1): 84, 44, 69, 0	mRuby-ChR (AMIGO1): 20, 16, 32, 60
Fig. 2	4	AMIGO1-YFP +GxTX-594 (48 hr): 85, 41, 69, 0			AMIGO1-YFP +ChR-mRuby: 18, 22, 28, 61		
Fig. 2	3	0 hr: 41, 35, 25		1.5 hr: 38, 39, 41		48 hr: 28, 17, 56	
Fig. 8	3	AMIGO1(-) (GxTX Ser27Pra-JP): 20, 12, 8			AMIGO1(+) (GxTX Ser27Pra-JP): 39, 20, 13		
	2	AMIGO1(-) (GxTX Ser13Pra-JP): 15, 55			AMIGO1(+) (GxTX Ser13Pra-JP): 7, 62		
Sup. Fig. 3	2	AMIGO2-YFP (0 hr): 28, 116	AMIGO2-YFP (48 hr): 59, 6	GxTX-594 (48 hr, AMIGO2): 59, 6	AMIGO3-YFP (0 hr): 117, 43	AMIGO3-YFP (48 hr): 109, 0	GxTX-594 (48 hr, AMIGO3): 109, 0
Sup. Fig. 3	2	AMIGO2-YFP +GxTX-594: 64, 1			AMIGO3-YFP +GxTX-594: 108, 0		
Sup. Fig. 5	3	AMIGO1(-): 1, 1, 1			AMIGO1(+): 1, 1, 1		

Supplemental Table 4. N-values for imaging experiments.